Qualifying Antibodies for Image-Based Immune Profiling and Multiplexed Tissue Imaging

Qualifying antibodies for image-based immune profiling and multiplexed tissue imaging

Qualifying antibodies for image-based immune profiling and multiplexed tissue imaging

Ziming Du[1,2]*, Jia-Ren Lin[2,3*], Rumana Rashid[1], Zoltan Maliga[2,3], Shu Wang[2,3,4], Jon C. Aster[1,2], Benjamin Izar[2,3,5,6], Peter K. Sorger[2,3,7] and Sandro Santagata[1,2,3,8,9]

Harvard Tumor Atlas Network

[1]Department of Pathology, Brigham and Women's Hospital, Harvard Medical School, Boston, MA

[2]Ludwig Center for Cancer Research at Harvard, Harvard Medical School, Boston, MA

[3]Laboratory of Systems Pharmacology, Harvard Medical School, Boston, MA

[4]Harvard Graduate Program in Biophysics, Harvard University, Boston, MA

[5]Department of Medical Oncology, Dana-Farber Cancer Institute, Boston, MA

[6]Broad Institute of MIT and Harvard, Boston, MA

[7]Department of Systems Biology, Harvard Medical School, Boston, MA

[8]Department of Oncologic Pathology, Dana Farber Cancer Institute, Boston, MA

[9]Department of Pathology, Boston Children's Hospital, Boston, MA

*Equal contribution

Running Title: Image-based immune profiling antibody validation

MeSH Heading/Keywords: FFPE, Pathology, Single-Cell Analysis, Immunotherapy, Immune profiling, PD-1, PD-L1, CTLA-4 Antigen

Financial Support: Dana-Farber/Harvard Cancer Center is supported in part by an NCI Cancer Center Support Grant P30-CA06516. This work is also funded by NIH grants U54-HL127365 and U2C-CA233262 to PKS and SS, and by the Ludwig Center at Harvard. SW is supported by a Molecular Biophysics Training Grant T32-GM008313.

Corresponding authors:
Sandro Santagata, Brigham and Women's Hospital, 60 Fenwood Road, HBTM 8002P, Boston, MA 02115; Telephone: 617-525-5686; email: ssantagata@bics.bwh.harvard.edu
Peter K. Sorger, Harvard Medical School, 200 Longwood Avenue, Warren Alpert Building, Room 440, Boston, MA 02115; Telephone: 617-432-6901; email: peter_sorger@hms.harvard.edu

Abstract: 143 words
Word Count: 15,710 (including main text, boxes 1-5, references, main figure legends and tables)
Tables: 2
Figures: 8
Supplementary Tables: 9
Supplementary Figures: 17
Supplementary Movies: 2

ABSTRACT

Spatially resolved, multiplexed tissue imaging makes it possible to characterize cell types and states in human resection specimens, xenografts and animal tissues. A growing number of tissue imaging methods applicable to standard formaldehyde fixed paraffin embedded (FFPE) tissue sections have been described, the vast majority of which rely on antibodies for antigen detection and mapping. This protocol focuses on methods for confirming the selectivity and specificity of such antibodies for constructing and validating antibody panels. Although we use tissue-based cyclic immunofluorescence (t-CyCIF) as an imaging approach, the antibody testing methods we described are broadly applicable. We demonstrate the protocol by assembling a 16-antibody panel designed to enumerate and localize T-cells and B-cells, macrophages, and cells expressing immune checkpoint regulators in tumor resection specimens and by showing how the panel performs in the identification of common and rare immune cell types in lung cancer.

INTRODUCTION

Tissue biopsies and resections are among the most widely acquired patient samples in medicine and their analysis by anatomic pathologists is the basis for differential diagnosis of many diseases and virtually all cases of cancer. Tissue imaging also plays an important role in many basic and translational studies in developmental biology, pathophysiology and drug development. In clinical practice, tissue samples are usually formalin-fixed and paraffin embedded (FFPE), sectioned and then stained with haemotoxylin and eosin (H&E) following protocols that have been in place for nearly a century. Molecular diagnosis of such samples is facilitated in a subset of cases by immunohistochemistry (IHC) and in a yet smaller subset of cases by RNA and DNA fluorescence in-situ hybridization (FISH). IHC of FFPE tissue typically provides data on the level of expression and spatial distribution of a single marker[1] although two marker IHC is occasionally used[2].

The recent development of highly multiplexed imaging technologies has raised the possibility of much deeper molecular analysis of human resection specimens. Methods that can be implemented on top of universal FFPE-based pathology workflows are particularly promising. In contrast to single-cell sequencing or flow cytometry of disaggregated tissues, highly multiplexed digital histology provides data on cell identity and morphology within a preserved tissue context. Highly multiplexed tissue imaging has many applications in basic and translational research, for example in the analysis of genetically engineered and xenografted mice, in zebrafish and in drosophila embryos as well as a wide range of other areas of investigation[3]. Multiplexed tissue imaging is likely to find wide application in the analysis of clinical trial specimens where tissue-sparing methods are highly valued and also in the clinical workflows used for diagnostic surgical pathology.

Some multiplexed tissue imaging methods involve optical imaging whereas others use laser or ion beam ablation followed by spectroscopy. Ablation methods include multiplexed ion beam imaging (MIBI) and imaging mass cytometry (IMC); these methods achieve a high degree of multiplexing using antibodies as reagents, metals as labels and mass spectrometry as a detection modality[4–6]. Methods such as CODEX[7], DNA exchange imaging (DEI)[8] and tissue-based cyclic immunofluorescence (t-CyCIF)[9,10] use fluorescence imaging and a variety of primary-secondary detection chemistry to detect antigen binding by primary antibodies; t-CyCIF is conceptually the

simplest in that it involves conventional secondary antibodies and fluorophore-conjugated primary antibodies to assemble highly multiplexed images in a sequential manner.

Multiple approaches have also been developed for spatially resolved, highly multiplexed imaging of RNA (spatial transcriptomics[11]), including fluorescent in situ sequencing (FISSEQ)[12,13], padlock probes and in situ target-primed rolling-circle amplification[14] and multiplexed error-robust fluorescence in situ hybridization (MERFISH)[15,16]. Analysis of RNA in clinical samples has the potential to directly utilize a rapidly growing body of genomic and molecular data, but it can also be problematic due to the lability of RNA and the complexities of standardizing pre-analytical variables in many clinical settings[17,18].

Recent interest in multiplexed histology in cancer is driven in part by the introduction of immune checkpoint inhibitors (ICIs), which are changing the treatment options for many solid and hematological malignancies[19,20]. ICIs function by disrupting cell-to-cell interactions in a cell non-autonomous manner and by activating normal tumor surveillance by the immune system. Knowing the numbers, types and locations of immune cells in the tumor microenvironment is thought to be essential for understanding mechanisms of action. The use of ICIs as first line therapeutic agents[21,22] and as neo-adjuvant therapies[23] is increasingly common: targeting the immune checkpoints mediated by CTLA-4 (cytotoxic T lymphocyte-associated antigen-4), PD-1 (programmed cell death-1 receptor) and PD-L1 (programmed cell death ligand 1) has been shown to elicit dramatic therapeutic responses in a range of cancers including advanced non-small-cell lung carcinoma, melanoma, renal-cell carcinoma, and Hodgkin lymphoma[24–30].

Even in the case of tumor types that are broadly ICI responsive (e.g. melanoma), not all patients benefit from existing drugs and there are many types of tumors (e.g. triple negative breast cancer) in which only sporadic responses are observed. Thus, predictive biomarkers are needed. These biomarkers are likely to involve multiplex panels that enable “immune profiling” to determine the abundance, locations and states of tumor-associated immune cells and the levels of expression of ICI ligands and receptors on immune and tumor cells. Relevant intracellular states for immune cells include degrees of activation and exhaustion[31], rates of proliferation, degree of apoptotic priming and levels of replication, metabolic and other stresses.

Multiplex flow cytometry suggests that a minimum of 12-14 cell surface markers is required for a basic enumeration of T and B cell subtypes. Identifying stromal and tumor cells and their states likely requires a similar number of immunofluorescence markers. In addition, multiple checkpoints are currently being targeted therapeutically: approved drugs exist against PD-1, PD-L1 and CTLA-4 and multiple Phase II/III trials are ongoing[32,33] for drugs targeting LAG3 (Lymphocyte-Activation Gene 3), TIM3 (T cell Immunoglobulin Mucin-3), and TIGIT (T-cell Immunoreceptor with Ig and ITIM Domains). Thus, biomarker discovery for ICIs will require the ability to rigorously enumerate cell types and states based on the levels of expression of 20-40 immunofluorescence markers[34–38]. Ideally, these measurements can be made using technical platforms that allow individual research teams to develop and test new "mix and match" assays for specific drug targets, immune cell populations, and tumor biomarkers.

Regardless of how antibody-antigen conjugates are detected, virtually all multiplexed tissue imaging (e.g. MIBI, IMC, CODEX, DEI, t-CyCIF, etc.) involves the use of primary antibodies. An extensive literature exists on the use of primary antibodies in research and clinical workflows and it is well established that specificity and reproducibility are influenced by a range of analytical factors[39] that include dilution, incubation conditions, type and extent of conjugation etc. Some commercially available antibodies work well and others poorly or not all. Ongoing assessment is also necessary to reaffirm the reliability of antibodies that do work, actively monitoring staining across tissue types and batches of reagent.

In this protocol, we focus on methods for constructing and validating antibody panels for immune profiling of human tumors with a focus on enumerating T-cell and B-cells, macrophages, and cells expressing immune checkpoint regulators. We discuss factors that impact the assembly of such a panel and present data for a 16-plex panel that enumerates canonical immune cell types (B cells, helper and cytotoxic T cells, regulatory T cells, NK cells, macrophages and dendritic cells) with the potential to differentiate among 65,000 states using binary gating. 37 of these antigen-defined states comprised greater than 0.5% of the total immune cell population in primary lung tumors (the tumor type used as a reference in the current work) of which 19 states are commonly encountered immune cell subtypes. However, rare cells were identified for about 10^3 distinct antigen combinations (**Supplementary Fig. 1**). The imaging method used in this protocol to construct and test antibody panels involves tissue-based

cyclic immunofluorescence (t-CyCIF)[9,10], an extension of older approaches to sequential assemble high-plex images using fluorophore inactivation and/or antibody stripping. However, our approaches are applicable to many other imaging methods and we anticipate that that primary antibodies tested by t-CyCIF can also be used in other tissue imaging approaches.

t-CyCIF constructs high-dimensional images by sequential 4-6 color immunofluorescence imaging on a conventional microscope and can be extended to at least 60 antigens. In general, we find that the fluorophore inactivation process (which is based on light and acid or base-catalyzed oxidation) substantially reduces auto-fluorescence and that signal-to-noise ratio often increases with cycle number. For most antibodies, the order of addition does not appear to be critical and preservation of immunogenicity and morphology is excellent. For some samples, we have demonstrated preservation of structure out to the limits of super-resolution optical microscopes (about 140 nm laterally)[9]. To date, we have tested primary antibodies against cell cycle regulators, signaling proteins and kinases, cell lineage markers, transcription factors, a wide array of cell state markers[9], and multiple immune markers (see https://www.cycif.org/ for details)[9,40,41]. Efforts are also underway to integrate multiplex immunofluorescence imaging with FISH, *in situ* mRNA profiling and DNA mutation detection[42,43,43,44] as part of a multi-parametric approach to tumor characterization and human tumor atlas construction.

Fluorescence imaging of tissue (including by t-CyCIF) is possible on a variety of conventional fluorescence microscopes but such microscopes generally have fields of view that are smaller than those achieved by custom slide scanners. In either case, the instruments must have appropriate filters, an automated stage holder for securing slides, and the ability to record and retrieve precise stage positions across successive imaging cycles. We routinely perform immune profiling using wide-field microscopes with air objectives having numerical apertures of NA~ 0.2 to 0.6, but higher resolution instruments such as confocal, deconvolution and structured illumination microscopes make it possible to capturing fine subcellular detail.

One advantage of t-CyCIF is that individual investigators can create their own panels without the need for special equipment, using widely available reagents in a mix and match approach that is adaptable to specific tissue types and scientific questions. It seems very likely that antibody panels developed using t-CyCIF will be applicable (perhaps with small modification such as differing dilution) to other high-dimensional multiplexing approaches, regardless of

instrumentation. It is also likely that the specific antibodies best suited to t-CyCIF will be largely the same as antibodies for IMC, MIBI, DEI and CODEX because antigen detection is fundamentally similar; the primary difference among these approaches involves the mode of detection (and thus, the atoms or molecules conjugated to the primary antibody).

The current protocol covers methods for immune panel assembly and validation that include slide staining, image acquisition, and data processing as well as multiple techniques for data visualization; these methods can be implemented by most laboratories familiar with immunofluorescence using a variety of microscopes. We describe development of a 16-marker panel for characterizing canonical immune cell types as well as the proliferation marker Ki-67, cell lineage markers GFAP (glial fibrillary acidic protein; an intermediate filament protein), α-SMA (alpha-smooth muscle actin), and a pan-isoform keratin epitope. In the anticipated results section below, we use this antibody panel to profile lung cancer samples, identifying multiple immune populations and visualizing their spatial distribution within tumors. We also show how imaging can be a superior technology for the detection of very rare immune cell subtypes that are hard to identify using flow cytometry. Imaging is highly advantageous in this regard in that the sample is preserved, making it possible to return to an unanticipated signal and to subject it to detailed visual and morphological analysis.

We envision that successful immune cell profiling will involve the ability to innovate quickly in the context of a torrent of new data on immuno-oncology as well as a commitment to the free and open sharing of information, reagents, methods, and computational tools, some of which will be reduced to practice by industry for general clinical use. Our group is developing an antibody validation resource at https://www.cycif.org/ comprising a list of reagents, images and caveats and a discussion of best practices; the site also describes data analysis, visualization and management software needed to construct pre-cancer and cancer atlases[45]. We are also performing cross-platform comparison to assist laboratories using MIBI, CODEX or DEI. We hope that instrument and antibody suppliers will respond to these academic efforts by manufacturing quality-controlled panels for clinical use.

Development of immune profiling panels

Box 1: Approaches to Antibody Testing and Qualification

There is no single approach to testing antibodies for tissue-based imaging, particularly in the case of human samples. Moreover, no antibody is ever fully "validated" since the pattern and intensity of staining is always subject to unknown confounders arising from pre-analytical variables encountered during sample acquisition and preparation[46,47] and from analytical variables encountered during sample processing and analysis. Instead, a variety of different approaches are needed depending on the sample and the antibody being studied. These approaches include (i) comparing patterns of staining by different antibodies on the same sample, which is particularly useful when highly qualified FDA-approved antibody reagents are available as comparators (e.g. anti PD-1 antibodies[48]), (ii) examining patterns of staining in tissues having stereotypical structures and spatial distributions of multiple cell types (e.g. immune cells in tonsil), and (iii) staining tissues with known genetic lesions such as HER2 over-expression or *CDKN2A* deletion. The later approach is particularly effective in the case of antibody panels for profiling mouse tissues; these panels can often be tested using genetically engineered mouse models (although we do not discuss this further in the current protocol).

Comparing Multiple Antibodies

Antibodies can be compared to each other at the level of pixels, cells or tissues (**Fig. 1**). In all cases, the starting point is an image in which different cycles of imaging have been correctly registered to each other. We have created the open-source *ASHLAR* algorithm (https://github.com/sorgerlab/ashlar) for joining together (stitching) successive image panels and then registering images across channels; *ASHLAR* improves on methods currently available in *ImageJ* (https://imagej.nih.gov/ij/) and is compatible with any image format complying with the *Bio-formats* standard[49–52].

a. Pixel-Level Analysis

The signals generated from two or more antibodies that selectively detect the same protein should, in principle, be highly correlated with each other down to the resolution of the microscope. This can be assessed by measuring the correlation between images at pixel resolution; image segmentation and morphological analysis are not necessary, and the analysis is therefore straightforward and objective. Pixel-level correlation analysis is the preferred method for comparing antibodies against the same antigen when labeling with different fluorophores is possible (this is straightforward when primary antibodies derive from different species). To

measure Pearson correlation on either a log or linear scale, antibodies are labelled with different fluorophores either by direct conjugation or using suitable secondary antibodies and images from different channels are then registered and compared directly.

b. Cell–Level Analysis

When fluorescence images are compared to IHC images or two different IHC antibodies are compared to each other, it is almost always necessary to use successive tissue slices. In this case, different cells are being stained and pixel level comparison is not meaningful. Instead, analysis usually involves image segmentation, binary scoring and then correlating the number of positive and negative cells across sections. However, matching morphologies and staining patterns across different cells is inherently more subjective than pixel-level analysis and, at the current state of the art, human judgement is often required (although the introduction of machine learning methods, which have demonstrated super-human performance in other medical imaging tasks[53], may change this).

Conventional computer-assisted cell-level analysis involves three sequential steps. First, cell boundaries are identified by computational segmentation, followed by integrating signal intensity across each cell, channel-by-channel, while subtracting background signal. Second, distributions are constructed for the integrated staining intensity in each channel and analyzed manually or automatically to score positive and negative populations. This yields a high-dimensional cell state vector in which both absolute intensities and correlations between these intensities are informative (e.g. a $CD4^+$ $CD8^+$ double thymocyte is different from a thymocyte positive for either marker alone). Third, correlations among state vectors for different cells are visualized using tools and methods such as multi-axis scatter plots, t-SNE plots, and X-shift plots. These approaches help to cluster cells with similar state vectors and lineage markers. More rigorous, multivariate statistical analyses can then be used to quantify the nature and degree of similarity or difference, for example by discriminant analysis[54] or principal components analysis[55]. Spatial analysis can also be performed to determine if different cell populations (cells whose state vectors are similar) have a particular spatial relationship to each other.

Additional analytical methods include computational analysis of cell and tissue morphology (e.g. to identify membranes, blood vessels or subcellular organelles and the cytoskeleton). For

simplicity, we do not describe these approaches and refer readers to methods for proximity analysis in multiplexed tissue described in the literature[9, 56].

c. Tissue-Level Analysis

Tissue-level analysis provides information on the spatial distribution of cells, cell state attributes, membranes, tissue boundaries and structures such as blood and lymphatic vessels. In computer-assisted tissue-level analysis, the positions (centroids) of individual cells are typically recorded, making it possible to revisit specific cells for further analysis or human inspection. Tissue level analysis is most effective for antibody testing and validation using tissues that have a stereotypical distribution of cell types. One of the most frequently used human tissues is tonsil; it contains a wide variety of immune cell types compartmentalized in primary lymphoid follicles and secondary lymphoid follicles with germinal centers (e.g. see https://www.proteinatlas.org/learn/dictionary/normal/tonsil); tonsils are also readily available under discarded tissue protocols and FFPE specimens are available from commercial vendors including Origene, Pantomics and GeneTex.

Tissue-level analysis of experimental samples typically involves the specification of regions of interest (ROIs), such as tumor and the non-neoplastic tissues surrounding the tumor, and calculation of relative levels staining in different ROIs. For example, the extent of tumor infiltration by immune cells is typically highly non-uniform, and immune cells are often substantially more abundant in an ROI corresponding to the tumor/stroma interface than the tumor interior. ROIs can be defined manually by pathologists based on classical morphological criteria following H&E staining. Tumor markers such as pan-keratin (an epitope shared among multiple keratin isoforms) or stromal markers such as alpha-smooth muscle actin make the identification of ROIs similar. In this protocol, we used an objective approach to ROI-definition based on a K-nearest neighbor (KNN) algorithm. The algorithm iteratively assesses whether a cell and its neighbors express tumor markers, assigning those that do to the tumor ROI and those that do not to non-neoplastic tissue.

End Box 1

Box 2: Tissue and Cells for Antibody Testing

Selecting an appropriate set of samples for any tissue imaging project is obviously of paramount importance, but it is beyond the scope of the current article; a discussion of factors affecting

study design and statistical analyses can be found elsewhere[57–59]. In general, a range of sample types is used for antibody validation including clinical specimens with known genetic alterations. For example, malignant peripheral nerve sheath tumors with *EED* or *SUZ12* mutations for testing antibodies against H3K27me3, or mismatch repair deficient tumors carrying inactivating alterations for testing antibodies against MSH2/MSH6 or MLH1/PMS2; in both instances there is a highly characteristic loss of signal in tumor cells with retention of signal in non-neoplastic (and genetically wild-type) stromal cells and neighboring normal tissues. Other FFPE tissue samples useful for antibody validation include specimens with known patterns of protein expression (e.g. breast or prostate cancer with expression of certain hormone receptors), or tissues containing cells from defined lineages (e.g. kidney/upper urinary tract and the Müllerian system for validating PAX8 antibodies, breast for GATA3 antibodies, and prostate for NKX3.1). Such FFPE validation samples can be compiled into tissue microarrays (TMAs) that allow investigators to not only assess sensitivity but also the specificity of the antibody reagents across dozens of normal and pathologic tissue types.

Other reagents commonly used for antibody validation include cell lines subjected to si/shRNA knockdown, CRISPR-Cas9 genome editing[60], ORF overexpression, drug or chemical exposure or environmental manipulation. Cultures of these cell lines are pelleted, fixed and embedded in FFPE blocks in the same manner as tissues; blocks with individual cell lines are then assembled into cell line microarrays (CMAs; see protocol below). Antibody can also be performed following conventional protocols for staining cultured cells (or following cell-based CyCIF)[61] but this is less ideal because of the impact of different fixation conditions on antibody performance.

When using any tissue or cell line bank for antibody testing, staining should be evaluated for subcellular localization (e.g. nucleus, membrane, endoplasmic reticulum, cytoplasm), cell type (e.g. tumor, stromal cells), strength of signal, signal to noise ratio, and dynamic range (e.g. **Supplementary Table 2**). During antibody validation, we typically initiate testing of fluorophore-conjugated antibodies at a concentration of 10 µg/ml and select a concentration for use that gives optimal signal strength and signal to noise ratio.

Creating FFPE Cell Microarrays (CMAs) for Antibody Testing

●**TIMING** **60 min**

! CAUTION Follow local biosafety guidelines for details on handling biohazardous materials

1. Assemble a suitable panel of genetically engineered or drug-treated cell lines.
2. Heat HistoGel (VWR, cat. no HG-4000-012) to 60 ºC to liquefy the solution.
3. Collect cells from a confluent T75 flasks or 10 cm dishes into a 15-ml falcon tube.
4. Centrifuge the samples at 200 *g* for 5 min.
5. Remove the supernatant.
6. Resuspend cell pellet in 500 µl of 4% phosphate buffered formaldehyde or 10% phosphate buffered formalin and fix at 4 ºC for 15 min.

   ▲**CRITICAL STEP** Do not over fix the samples which can affect antigen-antibody binding.
7. Centrifuge samples at 200 *g* for 5 min.
8. Remove the supernatant.
9. Resuspend cell pellet with 1 ml of PBS to wash.
10. Centrifuge the samples at 200 *g* for 5 min.
11. Remove PBS.
12. Cut off the distal end (1 cm) of a 1 ml pipette tip and gently resuspend the cell pellet in 300 µl of warm HistoGel.
13. Place the HistoGel with cells on a piece of parafilm to allow a droplet to form.
14. Incubate at 4 ºC for 1 h to allow the HistoGel droplet to harden.
15. Subject the HistoGel droplet to paraffin embedding to create a FFPE block.
16. Cut 5 µm sections from the FPPE tissue block and mount on slides.

▲**CRITICAL STEP** Do not leave the sample in HistoGel without further processing into paraffin blocks for longer than couple of days.

End Box 2

Box 3: Cell Type Identification

The identification of immune cell types is typically based on assessing the presence or absence of expression of CD (cluster of differentiation) and other cell surface markers as well as lineage-specific transcription factors. The binary (antigen positive or antigen negative) score across multiple markers identifies the cell type and the greater the number of markers, the more precise

the subtyping (e.g. $CD4^+$ $CD8^+$ staining identifies double positive T cells). The assumption is typically made that CD markers are present or absent depending on cell type. The multi-channel distribution of staining intensities for a cell therefore represents its identity convolved by measurement of noise and intrinsic cell-to-cell variability (**Fig. 1**). Calling immune cell types from image data in this manner starts with subtracting fluorescence signals arising from auto-fluorescence and nonspecific antibody binding, segmenting the image to identify individual cells and then integrating staining intensity over each cell.

a. Image Segmentation

Segmentation of images with densely packed cells is a challenging task, particularly when cells of different sizes and shapes are intermingled in tissues[62]. Segmentation is the focus of an entire subfield of machine vision[63,64] and new approaches that learn directly from pixel-level data (bypassing segmentation altogether) are also in development. The approaches described in this protocol represent a good starting point for high-dimensional image analysis, but they are among the simplest available; users may therefore wish to investigate other options. We typically apply standard watershed algorithms (in ImageJ or MATLAB; available at our GitHub repository: https://github.com/sorgerlab/cycif) to identify nuclei (of Hoechst 33342-stained nuclei imaged in the "DAPI" channel) and then dilate the nuclear mask to encompass a representative portion of the nucleus. Staining intensity is integrated over the cytoplasm, the nucleus or both compartments. Making masks slightly larger than a typical lymphocyte (~10 μm in diameter) is generally sufficient to quantify cell surface staining. A rolling-ball algorithm is used to remove global and regional background for each channel[9]. Evaluation of image segmentation and an assessment of the types of errors that typically occur is shown below in the Anticipated Results section (**Supplementary Fig. 2**).

b. Manual Gating to Identify Cells with Positive or Negative Staining

The intensity distribution obtained after image segmentation can be analyzed manually or automatically to identify positive and negative populations (**Fig. 1**, a manual gating example is shown in **Supplementary Fig. 3**). Manual gating is usually performed on one or two dimensions at a time, by pathologists or cell biologists who also review fluorescence images to assess staining patterns associated with different cut-off values. This is directly analogous to gating multi-dimensional flow cytometry data.

However, staining intensity for marker-positive and -negative populations is typically less well separated in segmented image data than in flow data. In addition, we have found that intensity distributions for CD markers (e.g. CD8a) can have more than two modes and these modes can vary across cell types. Other CD proteins are more highly expressed in some positive-scoring cell populations than others: (e.g. CD4 protein levels are substantially higher in T cells than in macrophages). Thus, it can be difficult to set a single cut-off value that effectively and reproducibly distinguishes cell types. This problem is compounded by pre-analytical variables such as cold ischemia time (the interval between when a sample is resected and the time it is placed in fixative) which can affect antigen preservation, differences in fixation time and processing, differences in the ages of the blocks (e.g. a sample resected one year before testing versus a sample resected a decade prior), or in the age of the sectioned tissue (e.g. a 'fresh' section that was cut from a paraffin block one day earlier versus one that was cut six months earlier and has been stored in ambient conditions). These factors are often called "pre-analytical variables" and have been studied extensively[65,66]. Analytical variables such as differences in antibody incubation time, imaging time (or instrument type) and resolution also affect gating. The practical consequence is that a single gate is often insufficient to determine marker positive and negative cell populations; instead, gates mush be adjusted for each sample manually, which is time consuming and potentially introduces biases in multi-sample analysis.

The relatively poor separation between marker-positive and -negative cells in many tissue images (relative to flow cytometry data) reflects the fact that simple integration of staining intensities across cells destroys much of the information in an image. More advanced methods for analyzing morphology, perhaps by direct learning from pixel-level data, are therefore required. The approaches described here should, therefore, be regarded as representing a reasonable first step in the complex process of cell-type calling from images.

c. Automated Gating Using Gaussian Mixture Modeling

Some of the liabilities associated with manual gating are addressed by automated gating using Gaussian mixture modeling (GMM). GMM fits high-dimensional Gaussian distributions to empirical distributions in the log domain under the assumption that data points are generated from a mixture of a finite number of Gaussian (normal) distributions with unknown parameters (means and standard deviations)[67]. Each Gaussian in the final mixture model is assumed to

correspond to a different cell population, providing an objective method for estimating the number of subpopulations and assigning each cell in an image to a specific positive, negative or intermediate marker value. The introduction of too many distributions (overfitting) is penalized by criteria such as likelihood ratios[68] or Bayesian Information Criterion (BIC)[69]. One limitation of GMM analysis is that it has limited ability to identify rare cell populations since the Gaussians corresponding to populations with few members are usually penalized and eliminated. Thus, GMM analysis and manual gating are complementary methods.

d. Marker Analysis

The procedures described above, and the cell level analyses described in **Box 1** have the advantage that they create multi-dimensional marker scores, cell position plots, etc. that are directly analogous to familiar flow cytometry data. Higher-order correlations among markers can, therefore, be visualized and analyzed using standard approaches such as clustering, multi-axis scatter plots, t-SNE plots[70], and X-shift plots[71].

Box 4: Practical Implementation of a 16-antibody Immune Marker Panel

To assemble a panel of antibodies for immune profiling, we used normal human tonsil (**Fig. 1**). For immune markers for which multiple antibodies were available, we performed pixel-by-pixel comparison across one or more cycles of t-CyCIF. As noted above, multi-channel fluorescence imaging is greatly superior to IHC in this setting because antibodies labelled directly or indirectly with different fluorophores can be mixed and used to stain a single tissue section. In other cases, we compared fluorescence and IHC images or used tissue-level data. The large numbers of fluorophore-conjugated antibodies available commercially for many immune markers make all three approaches useful.

a. Antibody Validation by Pixel-by-Pixel Comparisons

A single FFPE section of human tonsil was stained with four different commercially available antibodies raised against PD-1. This included two chemically conjugated antibodies, PD-1 clone EPR4877(2) conjugated to Alexa Fluor 647 (AF 647) and PD-1 clone NAT105 conjugated to Alexa Fluor 488 (AF 488) and two unconjugated antibodies, PD-1 clone EH33 (mouse) and PD-1 clone D4W2J (rabbit) (**Fig. 2** and **Supplementary Tables 1, 2**). EH33 and D4W2J detection involved indirect immunofluorescence with secondary antibodies: anti-rabbit (AF 647) for EH33 and anti-mouse (AF 555) for D4W2J.

We found that staining from all four antibodies co-localized to the plasma membrane of cells in tonsil germinal centers (**Fig. 2**), which are lymphoid structures that contain large numbers of follicular T helper cells known to express PD-1[72]. Pixel-by-pixel comparison of fluorescence intensities values showed that signals from three of the antibodies were highly correlated (Pearson correlation = 0.99), while the signal from clone NAT105 had a lower dynamic range and was less well correlated (Pearson correlation = 0.79-0.80; **Fig. 2**, and **Supplementary Table 2**). We interpreted the low correlation to be a consequence of non-selective antigen binding. We selected PD-1 clone EPR4877(2) for the immuno-profiling panel due to its wide dynamic range (14300 ± 5800 fluorescence intensity arbitrary units) and the availability of a t-CyCIF compatible fluorophore conjugated antibody (see below, Experimental design) (**Supplementary Tables 1, 2**).

Pixel-by-pixel comparison was also used to test other antibodies including three PD-L1 antibodies (**Supplementary Fig. 4**), two FOXP3 antibodies (**Supplementary Fig. 4**), three CD45 antibodies (**Supplementary Fig. 5**), five LAG3 antibodies (**Supplementary Fig. 6**), and three CD11b antibodies (**Supplementary Fig. 7**). In each case, antibodies selected for inclusion in the multiplex profiling panel were prioritized based on pixel-by-pixel correlation values with comparators, dynamic range, and the availability of fluorophore-conjugated antibodies (**Supplementary Tables 1, 2**).

b. Antibody Validation by Comparison to Established, Clinical-Grade IHC Antibodies

Sixteen of the most promising antibodies against immune cell markers (as determined from the multiple validation methods discussed in **Box 1**, shown in **Fig. 1** and indicated in **Supplementary Table 3**) were combined with pan-keratin, GFAP, α-SMA and Ki-67 antibodies in a 20 antibody panel that was then used for 9-cycle t-CyCIF staining of tonsil (**Table 1, Supplementary Table 3);** the panel was designed to distinguish immune subtypes, tumor cells and stromal cells and also to identify those cells of all types that were proliferating.

Patterns of t-CyCIF staining were compared with IHC staining patterns for eight antibodies (against CD3, CD4, CD8, CD20, CD68, PD-1, PD-L1 and FOXP3) that are routinely used for clinical diagnosis by the Anatomic Pathology service at Brigham and Women's Hospital; **Fig. 3**, **Supplementary Table 4**, and **Supplementary Fig. 8**) as well as by clinical services at other

medical centers. Such antibodies are the backbone of contemporary immune profiling[2]. As judged by two trained pathologists, the fluorescently conjugated and IHC antibodies showed similar patterns of staining; in particular, expected immune cell subtypes localized to the appropriate tonsil compartments in whole slide images. For example, small cells positive for CD20 staining were highly enriched in germinal centers, which contain many B cells, while CD4+ and CD8+ cells were found predominately in tissue surrounding the germinal centers, which contains many T cells (**Fig. 3**, and **Supplementary Fig. 8)**. Large, irregular CD68+ cells were enriched in germinal centers, which contain numerous macrophages phagocytosing B cells that are undergoing apoptosis. In addition, antibodies against Ki-67, CD19, CD14, CD163 and IBA1 exhibited staining consistent with the established intra-tissue distribution of cycling cells, B cells, and macrophages, respectively.

To quantify the fraction of cells positive for IHC staining in tissue sections adjacent to the section used for t-CyCIF, we used standard Aperio ImageScope software (Leica). We observed a high degree of correlation between the number of positive cells identified by IHC and by t-CyCIF for all eight markers for which comparison was possible. For this analysis, a total of ~288,000 cells were successfully segmented in the t-CyCIF data and ~80,000 to 237,000 cells were segmented from slides subjected to IHC. The Pearson correlation between the number of positive cells determined by IHC and by manual gating of t-CYCIF data across all eight markers was 0.98 (**Fig. 3**). A strong correlation was also observed when fluorescence intensity distributions were gated using GMMs (**Fig. 3**; Pearson correlation = 0.95).

c. Antibody Validation by Co-segregation of Markers Across a Tissue

Next, we performed tissue-level analysis by asking whether observed patterns of co-staining were consistent with prior knowledge of immune marker expression in specific sub-populations of immune cells found in human tonsil. To look for co-staining, intensity data for each segmented cell was visualized in two-way scatter plots (**Fig. 4; Supplementary Figs. 9-10** and **Supplementary Movie 1**). This analysis revealed co-segregation of markers such as PD-1 and CD3, CD8a and CD3, PD-L1 and IBA1, CD3 and CD45RB, and FOXP3 with both CD4 and CD3 (**Fig. 4**, and **Supplementary Fig. 9**). Moreover, we found that a subset of T cells co-expressed LAG3 and PD-1, a phenotype that is indicative of T cell exhaustion. Some cells co-

expressed CD163 and IBA, two markers of macrophage lineages. Taken together, pixel-level analysis, comparison of immunofluorescence staining with established IHC patterns and tissue-level analysis suggested that our profiling panel was selective and reproducible.

End Box 4

Box 5: Considerations for Assembling IF Antibody Panels

Once antibodies are individually qualified as described in the preceding boxes, an antibody panel is assembled for subsequent testing. This assembly involves several considerations:

1. To reduce errors, staining plans should include multiple overlapping (and even redundant) markers for defining each cell population. For example, cytotoxic T-cells are defined in our panel by co-expression of CD45, CD3, and CD8.

2. In the specific case of t-CyCIF, the first cycle can accommodate up to three unconjugated antibodies generated in three different host species (e.g. mouse, rabbit, goat, etc.); the fourth channel is used for Hoechst staining).

3. In t-CyCIF, subsequent cycle requires three antibodies that are conjugated to fluorophores. The fluorophores must have non-overlapping emission wavelength spectra; we recommend Alexa Fluor 488, Alexa Fluor 555, and Alexa Fluor 647.

4. It is best to avoid combining, within one cycle, antibodies that stain different epitopes on the same or similar structures where there are very different levels of signal intensity; in this case, channel bleed through may obscure the weaker signal.

5. Primary antibodies that are conjugated to fluorophores that are resistant to photo-inactivation such as Alexa Fluor 546, Alexa Fluor 568, and Alexa Fluor 594 should not be used for t-CyCIF due to signal carry-over between cycles. If necessary, primary antibodies conjugated to these fluorophores can be used in the final cycle of imaging when carry forward of signal is irrelevant.

6. Some types of phycoerythrin (PE) (e.g. Abcam PE-conjugated antibodies) emit signal in both the FITC and Cy3 channel and should be avoided.

END Box 5

Extension of the Profiling Panel to Additional Immune Cell Types

The 16-marker immune profiling panel describe in this paper (**Table 1**) includes widely expressed immune lineage markers (CD45, CD45RB), T cell markers (CD3, CD4, CD8, FOXP3), B cell markers (CD19, CD20), macrophage markers (CD68, CD163, IBA1, CD14, CD11b), and immune checkpoint markers that are expressed on T cells, macrophages and some tumor cells (PD-1, PD-L1, LAG3) (**Supplementary Table 3**). To image primary lung tumors and their metastases (described in Anticipated Results section below) our antibody panel also includes α-SMA to label stromal cells, pan-keratin to label cancer cells and GFAP to label glial cells, which are intermingled with tumor cells in brain metastases. For other applications, the thousands of commercially available fluorophore-conjugated antibodies represent an excellent resource for the creation of panels customized to different needs (the antibodies we have tested can be found at https://www.cycif.org/). Addition of such antibodies to a panel should involve testing as described in **Boxes 1-5** and application of "pillars" (standardized guidelines) for antibody qualification developed primarily for CLIA-certified immunohistochemistry laboratories[39,73–75] One of these pillars is inclusion of positive and negative controls in each staining run; such controls can include normal tissues such as tonsil, TMAs or CMAs (and small control arrays can potentially be added to each slide). For some antigens, stereotypical variability is also observed in each tissue (e.g. CD markers on T cells) and this can serve as an internal staining control.

Considerations in the Construction of Antibody Panels

Even when individual antibodies have been validated, and the guidelines described in **Box 5** have been considered, it is necessary to demonstrate that mixtures of antibodies perform as expected. When combined, some antibodies generate unexpected patterns of staining not observed with individual antibodies, and mixtures of many antibodies can exhibit substantial interference (a phenomenon best described in multiplex immuno-binding assays[76,77]). In addition, cyclic staining methods such as t-CyCIF are sensitive to factors that affect antigenicity across cycles. We, therefore, routinely perform a thorough assessment of the effects of mixing and cycle number on immunogenicity (see Figure 5 and 6 in Lin et al. 2018[9] for the design and interpretation of such experiments). In the case of ten antibodies tested in this work (CD14, CD163, CD20, CD3D, CD4, CD8a, CD68, FOXP3, IBA1 and Keratin), we found that the order of addition was not a critical variable for 8 of 10 but that anti-CD3 and anti-CD68 staining fell

with cycle number. This finding is consistent with our general observation that staining intensity falls with cycle number for about 20% of antibodies and for a further 20% of antibodies signal increases. In the case of antibodies that do not change in intensity, reproducibility across cycle number is high within a single slide and across slides processed in parallel. For most antibodies where signal changes with cycle number, it is possible to control this variable by processing all samples in parallel. Future work is focused on further mitigating the effects of cycle number by applying gating techniques and cell calling algorithms that are less sensitive to absolute signal intensity, use of TMA-based calibration standards on each slide and identification of antibodies that are stable to changes in their order of use.

To illustrate how we test the impact of cycle number on the staining by antibodies used in our immune profiling panel, we show data from eight sequential sections from a human tonsil (**Supplementary Table 5**). Antibodies were added in early and late rounds and signal intensity was measured from similar regions of the tissue, using the same image acquisition times. The correlation in staining intensity between early and late cycles was high for 8 of 10 antibodies (**Supplementary Table 6** and **Supplementary Figs. 11, 12**) but staining for anti-CD3 and anti-CD68 antibodies started to fall after cycle 5 (**Supplementary Table 6** and **Supplementary Figs. 11, 12**). When anti-CD3 and anti-CD68 antibodies were used only in early cycles, there was little evidence of batch to batch variability (**Supplementary Table 6**). Moreover, even with the most problematic antibodies, the localization of the signal did not change and only intensity varied.

When considered from the perspective of a single tissue sample, t-CyCIF can seem rather slow: in most cases, only one or two cycles (7 channels) of staining and imaging can be performed per day. However, a single operator can process 30 or more slides in parallel and image entire tissue sections of four or more square centimeters. On a per-cell basis, this throughput is high relative to other high-plex tissue imaging methods and other single-cell technologies such as scRNASeq. Moreover, as a practical matter, the analysis and interpretation of data remains the most time-consuming aspect of high-dimensional pathology studies, usually exceeding the time required for data collection.

Future Directions

In the future, we anticipate that human tissues will be studied using protein imaging, dissociated single cell RNA-seq and/or spatial transcriptomics in parallel[78]. Multi-modality approaches such as these could provide unprecedented insights into cellular phenotypes and disease processes. We also expect improvements in throughput; in the case of t-CyCIF this will involve increasing the number of channels imaged in each cycle so that fewer cycles are needed to construct deep profiles.

t-CyCIF PROTOCOL

Expertise Needed to Implement the Protocol

The methods described below, which focus on t-CyCIF, are all accessible to trained research assistants, graduate students and post-doctoral fellows, without extensive specialized experience in tissue imaging. However, experience with computational biology is typically needed to analyze the resulting data. Implementing these approaches on other platforms (e.g. MIBI, IMC, Dei, CODEX) depends largely on the availability of suitable labeled antibodies and users of these methods should contact the relevant manufacturers.

MATERIALS

Note that the t-CyCIF procedure described below involves dewaxing and antigen retrieval on a Leica Bond III automated slide processor; similar instruments are manufactured by Ventana or Dako and are commonly found in histopathology core facilities. t-CyCIF can also be performed following manual de-waxing and antigen retrieval (e.g. using microwaving slides in citrate buffer or using a pressure cooker)[9].

REAGENTS

- Human tonsil FFPE tissue and three human lung cancer FFPE tissues (LUNG-1-LN: lung adenocarcinoma metastasis to lymph node; LUNG-2-BR: lung squamous cell carcinoma metastasis to brain; LUNG-3-PR: primary lung squamous cell carcinoma) were accessed from the archives of the Department of Pathology, Brigham and Women's Hospital, Harvard Medical School, Boston.

! CAUTION All experiments involving human tissues should be performed in accordance with the relevant guidelines by local ethics committees and local biosafety guidelines for details on

handling biohazardous materials. This study was approved by the Institutional Review Boards (IRBs) of Brigham and Women's Hospital and Dana Farber Cancer Institute, Harvard Medical School.

- Antibodies for t-CyCIF and IHC (see the list of antibodies used in **Table 1, Supplementary Table 1, 3, 4**).
  ▲**CRITICAL STEP** Store the antibodies according to the manufacturer's instructions.
- HistoGel (VWR, cat. no HG-4000-012)
- Deionized water
- Formaldehyde (ThermoFisher Scientific, cat. no. 28906)
- Formalin (Sigma-Aldrich, cat. no. HT501128-4L)
- Pierce™ 20X Phosphate Buffered Saline (ThermoFisher Scientific, cat. no. 28348)
- UltraPure™ Glycerol (Life technologies, cat. no. 15514011)
- 30% Hydrogen peroxide solution, ACS grade, including stannate-containing compounds and phosphorus-containing compounds to stabilize the solution (Sigma-Aldrich, cat. no. 216763-500ML)
- Sodium hydroxide (Sigma-Aldrich, cat. no. 221465-500G)
  ! CAUTION Sodium hydroxide and hydrogen peroxide are toxic; wear protective personal equipment, such as a lab coat, gloves, mask, and glasses.
- Odyssey® Blocking Buffer in PBS 500 ml (LI-COR, cat. no. P/N 927-40003)
- Hoechst 33342 (25 mg) (Cell Signaling Technology, cat. no. 4082)
- Bond Dewax Solution (Leica, cat. no. AR9222)
- BOND Epitope Retrieval solution 1 (ER1) (Leica, cat. no. AR9961)

EQUIPMENT

- Platinum COVERSLIPS (24x50)/Cs (10oz) (American Master Tech Scientific, cat. no. GL2450)
- StainTray 10 Slide Tray (Black)/ea (American Master Tech Scientific, cat. no. LWS10BK)
- Tissue-Tek® Vertical 24 Slide Rack (American Master Tech Scientific, cat. no. LWS2124)
- Tissue-Tek Slide Staining Set - Dishes and Baths (American Master Tech Scientific, cat. no. LWS19)
- Ice box
- Portable 20,000 LUX Dimmable LED Bright Light Panel (Amazon, ASIN B078JCBW9S, UPC 691608324805)
- Covertiles (Leica, cat. no. S21.4611)
- Slide scanning microscope such as RareCyte CyteFinder (RareCyte Inc., USA)
- BOND RX machine (Leica, USA)
- Plasticware and glassware: 100 ml Glass graduated cylinders (e.g. American Master Tech Scientific, cat. no. LWG0726); 15-ml and 50 ml centrifuge tubes (Corning, cat. nos. 430790 and 430808); 5-ml, 10, 25, 50 ml Pipettes (Corning, cat. no. 4487-4490), micro-pipettes and tips

SOFTWARE

- Image J software (https://imagej.nih.gov/ij/); RRID: SCR_003070
- MATLAB software (https://www.mathworks.com/products/matlab.html); RRID:SCR_001622
- ASHLAR algorithm (https://github.com/sorgerlab/ashlar); RRID:SCR_016266
- viSNE algorithms from the CYT single-cell analysis package were obtained from Dana Pe'er's laboratory at Columbia University[70], and were run with MATLAB R2017a

- X-shift: VorteX 29-Jun-2017-rev2 was obtained from Garry Nolan's laboratory in Stanford University School of Medicine[71] (https://github.com/nolanlab/vortex/releases)

- Venn diagrams were made using online Venny 2.1 tool from Bioinfomatics for Genomics and Proteomics at the Spanish National Biotechnology (http://bioinfogp.cnb.csic.es/tools/venny/index.html)

REAGENT SETUP

PBS buffer solution (1X)

- Combine 50 ml of Pierce™ 20X Phosphate Buffered Saline (ThermoFisher Scientific, cat. no. 28348) with 950 ml deionized water. 1X PBS buffer can be prepared in advance and stored at room temperature (RT) for several weeks.

Hoechst solution

- Dilute 25 mg of Hoechst 33342 (Cell Signaling Technology, cat. no. 4082) in 10 ml deionized water to make 2.5 mg/ml stock solution and store at 4 ºC. To make a working solution, dilute stock solution in Odyssey® Blocking Buffer (1:1000) to stain DNA and mark nuclei.

▲**CRITICAL STEP** Hoechst working solution should be prepared immediately before use.

NaOH solution (1M)

- Combine 2 g of sodium hydroxide (Sigma Aldrich, cat. no. 221465-500G) with 50 ml deionized water in a 50-ml centrifuge tube. Vortex the solution to allow sodium hydroxide to dissolve completely. 1M NaOH can be prepared in advance and stored at RT.

Fluorophore inactivation (bleaching) solution

- Combine 25 ml 1X PBS, 4.5 ml 30% H_2O_2, and 0.8 ml 1M NaOH in a 50-ml centrifuge tube. The final working concentration is 4.5% H_2O_2 and 20 mM NaOH in PBS solution. 30 ml fluorophore bleaching solution is sufficient for four standard slides.

▲**CRITICAL STEP** Fluorophore bleaching solution should be prepared immediately before use.

! CAUTION Hydrogen peroxide is toxic; wear protective personal equipment such as lab coat, gloves, mask, and glasses.

Glycerol solution (10%)

- Prepare a 10% glycerol in PBS solution by combining 1 ml of UltraPure Glycerol (Life technologies, cat. no. 15514011) with 9 ml 1X PBS in a 15-ml centrifuge tube. 10% Glycerol in PBS can be prepared in advance and stored at RT for several weeks.

Antibody mixture for t-CyCIF

- Prepare the antibody mixture for t-CyCIF by diluting the antibodies of interest in Odyssey® Blocking Buffer according to their optimal concentrations (**Supplementary Table 1).**

▲CRITICAL STEP Keep at 4 ºC or on ice.

EQUIPMENT SETUP

Leica BOND RX Setup

- **Instrument setup** (see user manual for instrument-specific details)**:** 1. Bake slides at 60 ºC for 30 min; 2. Dewax with Bond Dewax Solution at 72 ºC; 3. Use Bond solution of HIER ER1 for antigen retrieval at 100 ºC for 20 min; 4. Block for 30 min with Odyssey® blocking buffer at RT; 5. Incubate secondary antibodies for 60 min at RT; 6. Incubate Hoechst solution for 30 min at RT.
- **Reagent setup:** 1. Fill chamber 1 with 30 ml of 1X PBS; 2. Fill chamber 2 with 7 ml of Odyssey® blocking buffer; 3. Fill chamber 3 with 2 ml of the appropriate secondary antibodies conjugated with Alexa Fluor–488, Alexa Fluor–555, or Alexa Fluor–647 diluted in Odyssey® blocking buffer (1:1000 v/v).

▲CRITICAL STEP Prior to the first cycle of t-CyCIF, a prestaining (blocking) step is performed by incubating tissues with a mixture of appropriate secondary antibodies so as to block non-specific binding sites in the tissue. Secondary antibodies are chosen based on the species and isotypes of the unconjugated antibodies used in the first t-CyCIF cycle. Anti-rabbit Alexa Fluor 555 and anti-mouse Alexa Fluor 647 secondary antibodies were used in this study.

▲CRITICAL STEP Avoid using Alexa Fluor 546, Alexa Fluor 568 or Alexa Fluor 594 conjugated secondary antibodies, as these fluorophores are resistant to bleaching.

Imaging on a RareCyte CyteFinder Slide-Scanning Microscope. A variety of fluorescent microscopes can be used to image slides. We have tested a Leica Aperio Digital Pathology Slide

Scanner, GE IN-Cell Analyzer 6000, GE OMX-SR Super-Resolution Microscope and GE Cytell Cell Imaging System; Hamamatsu, Nikon and other companies also manufacture suitable instruments. The principle requirements for these instruments are (i) the ability to acquire four (or more) channel images without spectral interference (ii) a stage that grasps slides firmly and consistently, and (iii) the ability to store and retrieve exact slide positions between cycles. The speed, resolution, signal-to-noise ratio and number of available fluorescence channels vary with the microscope. The Cytefinder used here is capable of six-channel whole-slide imaging and precise slide positioning (note that only four channels were used for the work described here). Imager 5 software (RareCyte Inc.) was used for data acquisition. Relevant optical information is as follows (note that the channels names are somewhat arbitrary):

- **Filter sets:** channels are referred to by the manufacturer as '**DAPI channel**' used for imaging Hoechst using an excitation filter having a peak of 390 nm and half bandwidth of 18 nm and an emission filter with a peak of 435 nm and half bandwidth of 48 nm; **488 channel** having a 475 nm / 28 nm excitation filter and 525 nm/ 48 nm emission filter; **555 channel** having a 542 nm / 27 nm excitation filter and 597 nm / 45 nm emission filter and **647 channel** having a 632 nm / 22 nm excitation filter and 679 nm / 34 nm emission filter.

- **Objective lenses:** using either a 10X (NA = 0.3) or 40 X (NA = 0.6) long-working distance objective.

PROCEDURE

FFPE slide pretreatment ● TIMING 3 h

! CAUTION Follow local biosafety guidelines for details on handling biohazardous materials

1 | Set up protocol and prepare reagents for Leica BOND RX for t-CyCIF as described above under *Leica BOND RX Setup*.

2 | Open the lids of the reagent chambers and insert the reagent chamber tray into the Leica BOND RX machine.

3 | Create a new study using the protocol from Step 1, add each slide to the study, and print labels for each slide. The BOND requires barcoded labels on all slides to process them.

▲**CRITICAL STEP** Center the slide stickers evenly so that the Leica BOND RX can scan the barcodes on the stickers correctly.

4 | Place all labeled slides onto a slide tray, cover the slides with Bond Universal Covertiles, and insert the slide tray into the machine.

▲**CRITICAL STEP** Place the Covertiles right side up by using the "Leica" etched on each Covertile as an orientation guide.

5 | The Leica BOND RX machine will scan the barcodes on the stickers of FFPE slides and reagent chambers. Check the label readings by hovering the mouse over the slide labels. If all of the slides have been recognized correctly, then click the START button to run the protocol. This will dewax slides and perform antigen retrieval.

■ **PAUSE POINT** Slides can be stored in 1X PBS at 4 ºC for several days after processing on the BOND. Ensure that the entire tissue is covered in 1X PBS; otherwise the tissue will dry our and yield poor results.

Pre-staining and background determination ● **TIMING 16 -24 h**

▲**CRITICAL STEP.** Slide pre-staining (blocking) and background signal determination is particularly important for tissues with high auto-fluorescence.

6 | Place slides flat in a container with the tissue facing up, and then gently pour fluorophore bleaching solution into the container to completely cover tissue. Place the container between two LED light panels (one LED panel above and one below) at RT for 45 min.

▲**CRITICAL STEP** The pre-bleaching step is critical for reducing autofluorescence in the tissue and to inactivate the fluorophores of the secondary antibody from the pre-staining step.

▲**CRITICAL STEP** Light sources that produce excessive heat can damage tissues. LED light sources are therefore preferable and large flat LED panels are now readily available at low cost (see Equipment list for preferred light panel).

▲**CRITICAL STEP** Completely immerse the tissue sections in fluorophore bleaching solution. During the subsequent bleaching process, bubbles will appear and gradually increase in size and number. This indicates that the oxidation reaction is proceeding as expected.

? TROUBLESHOOTING No bubbles in fluorophore bleaching buffer.

7 | Wash slides 4 times with 1X PBS at RT for 3 - 5 min per wash. Slides can be placed into a slide rack and lowered into a staining dish of PBS.

8 | Using the secondary antibodies used in the pre-staining procedure in Step 1 to cover all tissues and incubate in the dark at 4 ºC overnight to block non-specific binding.

▲CRITICAL STEP Do not use a hydrophobic barrier pen on the slides, as we have found that this adversely affects subsequent cycles.

▲CRITICAL STEP Be careful not to scratch the tissue with pipette tip when applying the antibody solution.

9 | Bleach the fluorophores for 45 min at RT as described in Step 6.

10 | Wash the slides 4 times with 1X PBS at RT, 3 - 5 min per wash.

▲CRITICAL STEP Wash the slides to remove the fluorophore bleaching solution completely which may affect subsequent t-CyCIF.

11 | Incubate slides with Hoechst solution (2.5 µg/ml) in the dark at RT for 10 min.

12 | Wash the slides 4 times with 1X PBS at RT for 3 - 5 min per wash.

13 | Mount coverslips onto slides with 200 µl of 10% glycerol in 1X PBS to prevent dehydration during imaging. Slowly position coverslips in the center of each slide and lower the slowly onto the slide to avoid producing bubbles between the coverslip and to prevent scratching tissues. Do not allow cover slip to overhang the edge of the slide. Dry excess liquid by gently pressing the long edges of the slide against a paper towel.

▲CRITICAL STEP. Wet-mounting and positioning cover slips takes some practice that should be undertaken initially using non-precious specimens.

14 | Load the slide into the slide scanner and image at four wavelengths to record the background signal.

▲CRITICAL STEP Typically only a portion of each slide is covered in tissue and only this region should be scanned; it is important to save this region of interest (ROI) in the imaging software so that precisely the same region can be imaged in subsequent rounds of t-CyCIF.

▲CRITICAL STEP Check images as they are being acquired and adjust exposure times to remain in a linear range.

? TROUBLESHOOTING Blurry images.

15 | After image acquisition remove cover slips by placing the slides in 1X PBS in a staining dish (which holds slides vertically) for 10 min and then slowly pull the slides vertically out of the solution allowing the coverslip to remain behind.

▲**CRITICAL STEP** De-coverslipping is another procedure that requires practice. Always allow coverslips to fall away through gravity. Do not push the coverslips as this will scratch and damage tissues. It may take longer time than the recommended 10 min for coverslips to detach.

16 | Wash the slides 4 times with 1X PBS at RT for 3 - 5 min per wash.

■ **PAUSE POINT** Slides may be stored in 1X PBS at 4 ºC for several days. Make sure the entire tissue is covered in 1X PBS; otherwise the tissue will dry out resulting in poor results in subsequent staining steps.

First round of t-CyCIF ● TIMING 16 -24 h

17 | Dilute up to three unconjugated primary antibodies from different species to the appropriate concentration in Odyssey® blocking buffer, cover all the tissue, and incubate in the dark at 4 ºC overnight.

▲**CRITICAL STEP** In the first round of t-CyCIF, unconjugated primary antibodies can be used. As in conventional immuno-fluorescence these antibodies must be from different species (e.g. rabbit, mouse, and rat) to allow for detection with species-specific secondary antibodies. The optimal dilution for primary antibodies must be optimized empirically; we usually test across a range of dilutions starting from 1:100 guided by manufacturer's recommendations. The times listed for antibody incubation can be adjusted empirically; we use long incubations at 4 ºC for convenience. See Lin et al.[9] and https://www.cycif.org/ (RRID:SCR_016267) for information on increasing the throughput of t-CyCIF experiments.

18 | Wash slides 4 times with 1X PBS at RT for 3 - 5 min per wash.

19 | Cover the tissue with secondary antibodies and incubate in the dark at RT for 2 h.

20 | Incubate with Hoechst solution (2.5 µg/ml) in the dark at RT for 10 min.

21 | Wash slides 4 times with 1X PBS at RT for 3 - 5 min per wash.

22 | Mount coverslips onto slides with 200 µl of 10% glycerol in PBS and image the saved ROI for each slide with RareCyte CyteFinder as described in **Steps 13 and 14**.

▲**CRITICAL STEP** Use the saved ROI in the imaging software so that the exact same region of tissue is imaged for every cycle of t-CyCIF.

? TROUBLESHOOTING Blurry images.

? TROUBLESHOOTING Weak signal.

? TROUBLESHOOTING Saturating signal.

23 | After imaging, remove the coverslips and wash the slides 4 times with 1X PBS at RT for 3 - 5 min per wash.

24 | Perform fluorophore bleaching for 45 min at RT as described in **Step 6**.

25 | Wash slides 4 times with 1X PBS at RT for 3 - 5 min per wash

▲**CRITICAL STEP** Wash slides thoroughly to remove fluorophore bleaching solution since carry-over can adversely affect subsequent t-CyCIF cycles.

■ **PAUSE POINT** Slides may be stored in 1X PBS at 4 ºC for several days. Make sure the entire tissue is covered in 1X PBS. Otherwise, the tissue may become dry and yield poor staining results.

Cycles of t-CyCIF ● TIMING 16 -24 h per cycle

! CAUTION The maximum number of cycles for t-CyCIF depends on tissue type, which is evaluated by counting nuclei in the Hoechst channel. We are able to perform >10 cycles for most tissue types and >20 cycles for some resilient tissues, such as tonsil.

26 | Dilute up to three conjugated antibodies with different fluorophores in Odyssey® blocking buffer. Cover all tissue with antibody solution and incubate in the dark at 4 ºC overnight.

▲**CRITICAL STEP** Normally, Alexa Fluor 488, Alexa Fluor 555, and Alexa Fluor 647 conjugated primary antibodies are used. Antibodies dilution is optimized empirically starting from 1:100.

▲**CRITICAL STEP** Avoid using Alexa Fluor 546, Alexa Fluor 568, and Alexa Fluor 594 conjugated secondary antibodies, as these fluorophores are difficult to bleach.

27 | Wash the slides 4 times with 1X PBS at RT for 3 - 5 min per wash.

28 | Incubate with Hoechst solution (2.5 µg/ml) in the dark at RT for 10 min.

29 | Wash the slides 4 times with 1X PBS at RT for 3 - 5 min per wash.

30 | Mount coverslip onto slides with 200 µl of 10% glycerol in PBS and image the saved ROI with the RareCyte CyteFinder as described in **Steps 13 and 14**.

31 | Remove the coverslips as described in **Step 15**.

32 | Wash the slides 4 times with 1X PBS at RT for 3 - 5 min per wash.

33 | Bleach the fluorophores for 45 min at RT as described in **Step 6.**

34 | Wash the slides 4 times with 1X PBS at RT for 3 - 5 min per wash.

35 | Start next t-CyCIF cycle: repeat t-CyCIF cycles (cycles of **Step 26** to **Step 34**).

? TROUBLESHOOTING Blurry images.

? TROUBLESHOOTING Weak signal.

? TROUBLESHOOTING Saturating signal.

? TROUBLESHOOTING Cell loss.

? TROUBLESHOOTING Signal present after fluorophore bleaching step.

Image processing ● TIMING variable.

The data described here was obtained using pre-processing, registration, segmentation, and quantification software in Image J (scripts provided in Sorger Lab GitHub repository https://github.com/sorgerlab/cycif). As noted in the introduction, many potentially better tools are also available.

▲CRITICAL STEPS In steps 36 through 38 change the parameters in the script to account for the directory and names of the image files, the start and end cycle numbers, and the number of rows and columns used to create montages.

36 | Run the script named 1_Macro-SAVEALLCYCLES.ijm on ImageJ to perform background subtraction, flat-field correction, and save .tif images of individual tiles from the.rcpnl file generated by RareCyte CyteFinder for each cycle.

37 | Run the script named 2_Macro-imagereg-forRareCyte.ijm to perform registration of each tile using the Hoechst signal and a rigid body transformation algorithm. The registration information is applied to all channels of all images from each t-CyCIF cycle to generate a hyperstack of images from all cycles.

38 | Run the script named 3_Macro-CycIF-wholeslidequan.ijm to segment cells using the Hoechst signal from the last cycle, measure the average intensity of every marker for each cell, and output the data as a .cvs file for each image tile.

▲**CRITICAL STEP** Use the Hoechst image from the final cycle to generate a mask.

High Dimension Data Analysis and Visualization ● TIMING variable

39 | Run CycIF_readwholeslide.m to import the single cell data generated by Step 38 into MATLAB.

40 | Identifying specific cell populations

A. (Optional) Gaussian mixture models: Gaussian mixture models (GMM) are fitted using the Expectation Maximization (EM) algorithm in MATLAB. For each GMM, at least 80 different initial guesses are used as starting points for EM algorithm to find the maximum likelihood fit.

B. Manual gating: Cut-off values are set for each marker by a trained user by reviewing intensity distributions and florescence images.

41 | Heatmaps were generated using the intensity data for particular marker and location information of the cells (Xt, Yt) using MATLAB R2017a. By applying cut-off value for particular markers dot plots can be generated for various markers.

42 | Cluster plots, cross-correlation plots and scatter plots were generated from intensity data using MATLAB R2017a.

43 | Analysis by t-Distributed Stochastic Neighbor Embedding (t-SNE) analysis was performed using the viSNE implementation from the CYT single-cell analysis package[70] and run in MATLAB R2017a.

44 | (Optional) X-shift was performed using VorteX 29-Jun-2017-rev2 obtained from the Nolan lab (Stanford University School of Medicine; https://github.com/nolanlab/vortex/releases). (plots not shown)

45 | **(**Optional) Venn diagrams: Venn diagrams were generated using the online Venny 2.1 tool from the Bioinfomatics for Genomics and Proteomics Service at the Centro Nacional de Biotecnologia (CNB) in Spain (http://bioinfogp.cnb.csic.es/tools/venny/index.html). (diagrams not shown)

? TROUBLESHOOTING

Troubleshooting advice can be found in **Table 2**.

● TIMING

Steps 1-5, FFPE slide(s) pretreatment: 3 h

Steps 6-16, Pre-staining and background recording: 16 - 24 h

Steps 17-35, t-CyCIF cycles: 16 -24 h per cycle times 9 cycles

Steps 36-38, Image processing: variable

Steps 39-45, High dimension data analysis and visualization: variable

Box 3, Preparation of cell lines that have undergone perturbations for t-CyCIF validation in FFPE sections: 60 min

ANTICIPATED RESULTS

Immune Profiling of Lung Cancer Samples

We analyzed three human primary and metastatic lung carcinoma specimens to demonstrate the performance of the immune profiling panels validated and assembled according the guidelines described in this protocol. The tissues represent contexts typically encountered when evaluating malignancies; a lymph node metastasis (LUNG-1-LN), a brain metastasis (LUNG-2-BR) and a primary lung tumor (LUNG-3-PR), each from a different patient. We performed nine-cycle t-CyCIF in parallel on the three specimens followed by image segmentation, computational analysis and visual review by board-certified pathologists (**Figs. 5-8**, **Supplementary Figs. 13-17**, **Supplementary Tables 7-9** and **Supplementary Movie 2**). We then enumerated and mapped high and low frequency immune cell types.

The antibodies described in **Supplementary Table 3** generated staining at intensities sufficiently above background to enable manual and automated analysis. Manual review of images overlayed with segmentation masks revealed an overall accuracy of 80% ± 2% for computer-based cell identification, with visual analysis by a pathologist serving as the gold standard. We recognized three types of errors: cells that were missed by the segmentation algorithm, fusion of two or more cells into a single segmented entity, and splitting of a single cell between two or more entities (**Supplementary Fig. 2**). Segmentation accuracy was similar in cancer samples and

tonsil, but the types of errors differed between the types of samples; artefactual fusion of densely packed lymphocytes in tonsil was common whereas as tumor cells in lung cancer specimens (which are larger than lymphocytes) tended to be split. We do not yet know if these errors are random or systematic and their effects on cell has not been evaluated. However, it should be noted that the segmentation methods we applied are standard functions in *ImageJ*; more sophisticated segmentation algorithms using machine learning or multiple-features approaches (including nuclear, cytosolic or membrane markers) are very likely to improve segmentation accuracy. Machine learning from pixel-level data, which avoids the need for image segmentation altogether (and has been shown to yield super-human performance in other medical imaging applications[79]) is another possibility.

In **Fig. 5a**, we show the immunofluorescence signal from a section of the primary lung tumor specimen (LUNG-3-PR) that demonstrates the expression of four antigens: α-SMA (green), pan-keratin (blue), and CD45 or IBA1 (both red). A yellow box highlights a frame shown at high power in **Fig. 5e** (a representative merged image of pan-keratin (green), Ki-67 (white) and PD-L1 (red)). An image from this region, of an H&E stain from an adjacent serial section, is also shown (**Fig. 5f**). To generate a map of cell positions, we integrated staining intensity over each successfully segmented cell across the image (following background subtraction) and used the information to call out distinct cell types: α-SMA high cells were labeled stromal cells, pan-keratin high cells as tumor, and cells with CD45 or IBA1 as immune cells. Dots mark the computed centroid of each cell and the colors represent each cell's identity (**Fig. 5b** and **Supplementary Fig. 14**). In subsequent figures (**Figs. 7** and **8**), we use multiple markers to define distinct cell states and present their location in cell position plots. To facilitate visualization and assessment of the relative expression levels of individual antigens, we also generated intensity maps across the image; such maps are shown for keratin in **Fig. 5c** and PD-L1 in **Fig. 5d**. In the case of PD-L1, the maps reveal substantial spatial heterogeneity of PD-L1 expression in the tumor cell compartment (**Fig. 5d-f,** and **Supplementary Table 7**) suggesting dynamic and variable effects on immune surveillance. We also found that proliferating tumor cells, immune cells, and fibroblast populations were also unevenly distributed, revealing additional forms of heterogeneity. Interestingly, the extent of proliferation of non-tumor cells within the tumor microenvironment equaled or surpassed that of tumor cells (**Supplementary**

Table 7) suggesting that proliferation of stromal, non-neoplastic elements is ongoing in the tumors we examined.

We then used t-Distributed Stochastic Neighbor Embedding (**t-SNE**)[1, 3] to visualize and characterize the immune cell infiltrates from the tumor sections. t-SNE projects the 15-dimensional vectors of integrated staining intensity for each cell onto two dimensions in a manner that optimally preserves high dimensional relationships. We performed t-SNE on 2,000 randomly selected immune cells from each of the three lung cancer specimens. This showed that the immune cells clustered by specimen (LUNG-1-LN, LUNG-2-BR, LUNG-3-PR; **Fig. 5g** and **Supplementary Fig. 15**), revealing dramatic specimen-specific differences in resident immune cell populations. When we projected the levels of expression of specific immune cell markers onto the t-SNE plots (**Fig. 5g** and **Supplementary Fig. 15**), we found that the brain metastasis (LUNG-2-BR) had few $CD8^+$ T cells but many myeloid-derived immune cells (IBA1+/CD163+). In contrast, the primary lung tumor (LUNG-3-PR) was enriched in B cells (CD45+/CD20+) and T regulatory cells (CD45+/CD3+/CD4+/FOXP3+). The lymph node metastasis (LUNG-1-LN) was enriched specifically in CD45+/CD3+/$CD8^+$ T cells (**Fig. 5h** and **Supplementary Table 8**). Thus, the immune environments of these tumors are very different, presumably reflecting tumor-intrinsic differences as well as differences in the location of the tumor at the time of resection.

Identifying and Mapping Low Frequency Immune Cell Types

Many aspects of the tumor immune microenvironment remain enigmatic. A comprehensive understanding of the effects of the microenvironment on tumorigenesis and on response to therapy is likely to involve characterizing both high and low frequency immune cell populations. Highly multiplexed imaging is a potentially powerful way to identify rare cell immune types because it provides data not only on marker expression, but also on cell morphology and environment. Moreover, cells that represent outliers in biomarker distributions can be revisited for visual re-review to confirm their presence and potentially even for additional t-CyCIF analysis. In contrast, such re-review is not possible with flow cytometry data.

In our samples, multi-axis scatter plots of the three lung cancer cases revealed three very low-frequency immune cell populations: (i) CD8-expressing FOXP3+ regulatory T cells (CD45+/CD3+/CD4-/CD8a+/FOXP3+ cells) which represented 0.01 – 0.66% of all immune cells (ii) CD8-expressing LAG3/PD-1 double positive T cells (CD45+/CD3+/CD4-/CD8a+/PD-

1+/LAG3+ cells) which represented 0.01% - 0.97% of all immune cells) and (iii) CD4 expressing LAG3/PD-1 double positive T cells (CD45+/CD3+/CD4+/CD8a-/PD-1+/LAG3+ cells) which represented 0.03 – 0.08% of all immune cells **(Fig. 6, 7**, **Supplementary Fig. 16, 17** and **Supplementary Table 8**).

CD8-expressing FOXP3+ regulatory T cells (CD45+/CD3+/CD4-/CD8a+/FOXP3+ cells) have been reported previously in both human and mouse lymph nodes, spleen and blood as well as in prostate cancer and hepatocellular carcinoma and have been implicated in immune evasion and consequent disease progression[80–82]. We confirmed by visual review the presence of small round cells with lymphocyte morphology that were clearly positive for CD45, CD3, FOXP3 and CD8 (marked with red dots and boxes in **Fig. 6c, d**) and negative for CD4; the presence of nearby cells staining positive for CD4 (marked in green) provided an internal positive control for CD4 staining (**Fig. 6c, d**). Compared to directly adjacent non-neoplastic lung tissue in the histologic section, both automated and manual analysis showed that this rare cell population was 6-fold enriched in the tumor component ($p < 0.0001$; t-test). Conventional regulatory T cells (which are FOXP3+/CD4+/CD8-) were also enriched in the tumor region, but to a lesser extent (2.3- fold; $p < 0.001$; t-test) (**Fig. 7e,f** and **Supplementary Table 9**).

Similarly, double positive PD-1/LAG3 cells (CD45+/CD3+/CD4-/CD8a+/PD-1+/LAG3+ cells and CD45+/CD3+/CD4+/CD8a-/PD-1+/LAG3+ cells) were substantially enriched in the tumor region. The ~ 1% of immune cells that were CD8+/PD-1+/LAG3+ were 14-fold more abundant in the tumor region ($p < 0.0001$) and the ~0.1% of immune cells that were CD4+/PD-1+/LAG3+ were found essentially exclusively in the tumor ($p < 0.0001$; t-test) (**Fig. 7** and **Supplementary Table 9**). CD8+ T cells double positive for PD-1 and LAG3 have been described previously in tumor-bearing animal models and shown to have an exhausted phenotype;[83] they have also been found in human ovarian and triple-negative breast cancer resections.[84,85] However, the rarer CD4+ subtype is largely unexplored.

Multiplex imaging can also be used to identify truly rare cells. A surprising number of marker combinations currently undescribed in the literature can be observed in tissue biopsies[86]. For example, systematic assessment of PD-1+ cells in the LUNG-3-PR specimen revealed the presence of cells with 21 different marker combinations at a frequency of 3 cells per 2,000 or greater (**Fig. 8a**). We confirmed the presence of these unusual marker combinations by visual

inspection of the cells (**Fig. 8b** and galleries of images in **Supplementary Fig. 17**). However, whether these rare types of cells represent intermediates in the differentiation of known cell types or have unique and undescribed functions remains unknown.

Together, the data presented in this Anticipated Results section show how multiplexed tissue imaging can be used to enumerate common, low frequency and very rare immune cell subtypes in stromal and tumor tissue. In this application, imaging has two advantages over flow cytometry: (i) the locations of cells types is preserved with respect to each other and the overall architecture of the tissue or tumor (ii) visual review can be used to confirm that outliers in marker distributions in fact represent cells in which the markers have the expected spatial distribution, thereby increasing confidence that the cell type is real.

DATA AVAILABILITY

The datasets generated during and/or analysed during the current study are available to view on OMERO (https://omero.hms.harvard.edu/webclient/?show=project-2911). The raw data is available from the corresponding author upon request.

CODE AVAILABILITY

Custom codes used to analyze data in this study are available on GitHub (https://github.com/sorgerlab/cycif).

AUTHOR CONTRIBUTIONS

S.S. and P.K.S. supervised the project; S.S., J.L., B.I., J.C.A and P.K.S. were involved in planning; Z.D and J.L. performed the experiments and data analysis; R.R. S.W., and Z.M. contributed to data collection and analysis. All authors wrote and reviewed the paper.
Note: Any Supplementary Information and Source Data files are available in the online version of the paper.

ACKNOWLEDGEMENTS

This work was funded by U54-CA225088 to P.K.S. and S.S. and by U2C-CA233262 and the Ludwig Center at Harvard to P.K.S., J.C.A., and S.S.. We thank MP Wu, G Baker, Y Chen, J Muhlich, S Mei, and C Yapp for their expert assistance.

COMPETING INTERESTS

P.K.S. is a member of the Board of Directors of RareCyte Inc., which manufactures the slide scanner used in this study, and is a co-founder of Glencoe Software, which contributes to and supports the open-source OME/OMERO image informatics software used for image visualization in this work. S.S. has consulted for RareCyte Inc. The other authors of this study have no competing financial interests to disclose.

REFERENCES

1. Cyriac, G. & Gandhi, L. Emerging biomarkers for immune checkpoint inhibition in lung cancer. *Semin. Cancer Biol.* (2018). doi:10.1016/j.semcancer.2018.05.006
2. Tsujikawa, T. *et al.* Quantitative Multiplex Immunohistochemistry Reveals Myeloid-Inflamed Tumor-Immune Complexity Associated with Poor Prognosis. *Cell Rep* **19**, 203–217 (2017).
3. Willis, R. A. The borderland of embryology and pathology. *Bull N Y Acad Med* **26**, 440–460 (1950).
4. Giesen, C. *et al.* Highly multiplexed imaging of tumor tissues with subcellular resolution by mass cytometry. *Nat Meth* **11**, 417–422 (2014).
5. Angelo, M. *et al.* Multiplexed ion beam imaging of human breast tumors. *Nat. Med.* **20**, 436–442 (2014).
6. Keren, L. *et al.* A Structured Tumor-Immune Microenvironment in Triple Negative Breast Cancer Revealed by Multiplexed Ion Beam Imaging. *Cell* **174**, 1373-1387.e19 (2018).
7. Goltsev, Y. *et al.* Deep profiling of mouse splenic architecture with CODEX multiplexed imaging. *bioRxiv* 203166 (2017). doi:10.1101/203166
8. Wang, Y. *et al.* Rapid Sequential in Situ Multiplexing with DNA Exchange Imaging in Neuronal Cells and Tissues. *Nano Lett.* **17**, 6131–6139 (2017).
9. Lin, J.-R. *et al.* Highly multiplexed immunofluorescence imaging of human tissues and tumors using t-CyCIF and conventional optical microscopes. *Elife* **7**, (2018).
10. Gerdes, M. J. *et al.* Highly multiplexed single-cell analysis of formalin-fixed, paraffin-embedded cancer tissue. *Proc. Natl. Acad. Sci. U.S.A.* **110**, 11982–11987 (2013).

11. Ståhl, P. L. *et al.* Visualization and analysis of gene expression in tissue sections by spatial transcriptomics. *Science* **353**, 78–82 (2016).
12. Lee, J. H. *et al.* Highly multiplexed subcellular RNA sequencing in situ. *Science* **343**, 1360–1363 (2014).
13. Lee, J. H. *et al.* Fluorescent in situ sequencing (FISSEQ) of RNA for gene expression profiling in intact cells and tissues. *Nat Protoc* **10**, 442–458 (2015).
14. Larsson, C., Grundberg, I., Söderberg, O. & Nilsson, M. In situ detection and genotyping of individual mRNA molecules. *Nat. Methods* **7**, 395–397 (2010).
15. Chen, K. H., Boettiger, A. N., Moffitt, J. R., Wang, S. & Zhuang, X. RNA imaging. Spatially resolved, highly multiplexed RNA profiling in single cells. *Science* **348**, aaa6090 (2015).
16. Moffitt, J. R. *et al.* High-performance multiplexed fluorescence in situ hybridization in culture and tissue with matrix imprinting and clearing. *Proc. Natl. Acad. Sci. U.S.A.* **113**, 14456–14461 (2016).
17. Stewart, J. P. *et al.* Standardising RNA profiling based biomarker application in cancer-The need for robust control of technical variables. *Biochim. Biophys. Acta* **1868**, 258–272 (2017).
18. True, L. D. Methodological requirements for valid tissue-based biomarker studies that can be used in clinical practice. *Virchows Arch.* **464**, 257–263 (2014).
19. Wei, S. C., Duffy, C. R. & Allison, J. P. Fundamental Mechanisms of Immune Checkpoint Blockade Therapy. *Cancer Discov* **8**, 1069–1086 (2018).
20. Sharma, P. & Allison, J. P. Immune checkpoint targeting in cancer therapy: toward combination strategies with curative potential. *Cell* **161**, 205–214 (2015).
21. Socinski, M. A. *et al.* Atezolizumab for First-Line Treatment of Metastatic Nonsquamous NSCLC. *N. Engl. J. Med.* **378**, 2288–2301 (2018).
22. Carbone, D. P. *et al.* First-Line Nivolumab in Stage IV or Recurrent Non-Small-Cell Lung Cancer. *N. Engl. J. Med.* **376**, 2415–2426 (2017).

23. Forde, P. M. *et al.* Neoadjuvant PD-1 Blockade in Resectable Lung Cancer. *N. Engl. J. Med.* **378**, 1976–1986 (2018).
24. Topalian, S. L. *et al.* Survival, durable tumor remission, and long-term safety in patients with advanced melanoma receiving nivolumab. *J. Clin. Oncol.* **32**, 1020–1030 (2014).
25. Topalian, S. L. *et al.* Safety, activity, and immune correlates of anti-PD-1 antibody in cancer. *N. Engl. J. Med.* **366**, 2443–2454 (2012).
26. Ansell, S. M. *et al.* PD-1 blockade with nivolumab in relapsed or refractory Hodgkin's lymphoma. *N. Engl. J. Med.* **372**, 311–319 (2015).
27. Leach, D. R., Krummel, M. F. & Allison, J. P. Enhancement of antitumor immunity by CTLA-4 blockade. *Science* **271**, 1734–1736 (1996).
28. Pardoll, D. M. The blockade of immune checkpoints in cancer immunotherapy. *Nat. Rev. Cancer* **12**, 252–264 (2012).
29. Weber, J. S. *et al.* Nivolumab versus chemotherapy in patients with advanced melanoma who progressed after anti-CTLA-4 treatment (CheckMate 037): a randomised, controlled, open-label, phase 3 trial. *Lancet Oncol.* **16**, 375–384 (2015).
30. Gulley, J. L. *et al.* Avelumab for patients with previously treated metastatic or recurrent non-small-cell lung cancer (JAVELIN Solid Tumor): dose-expansion cohort of a multicentre, open-label, phase 1b trial. *Lancet Oncol.* **18**, 599–610 (2017).
31. Jiang, Y., Li, Y. & Zhu, B. T-cell exhaustion in the tumor microenvironment. *Cell Death Dis* **6**, e1792 (2015).
32. Baumeister, S. H., Freeman, G. J., Dranoff, G. & Sharpe, A. H. Coinhibitory Pathways in Immunotherapy for Cancer. *Annu. Rev. Immunol.* **34**, 539–573 (2016).
33. Kim, J. E. *et al.* Combination Therapy with Anti-PD-1, Anti-TIM-3, and Focal Radiation Results in Regression of Murine Gliomas. *Clin. Cancer Res.* **23**, 124–136 (2017).

34. Bendall, S. C. *et al.* Single-cell mass cytometry of differential immune and drug responses across a human hematopoietic continuum. *Science* **332**, 687–696 (2011).
35. Chevrier, S. *et al.* An Immune Atlas of Clear Cell Renal Cell Carcinoma. *Cell* **169**, 736-749.e18 (2017).
36. Lavin, Y. *et al.* Innate Immune Landscape in Early Lung Adenocarcinoma by Paired Single-Cell Analyses. *Cell* **169**, 750-765.e17 (2017).
37. Korin, B., Dubovik, T. & Rolls, A. Mass cytometry analysis of immune cells in the brain. *Nat Protoc* **13**, 377–391 (2018).
38. Fung, E., Esposito, L., Todd, J. A. & Wicker, L. S. Multiplexed immunophenotyping of human antigen-presenting cells in whole blood by polychromatic flow cytometry. *Nat Protoc* **5**, 357–370 (2010).
39. Bordeaux, J. *et al.* Antibody validation. *BioTechniques* **48**, 197–209 (2010).
40. Coy, S. *et al.* Multiplexed Immunofluorescence Reveals Potential PD-1/PD-L1 Pathway Vulnerabilities in Craniopharyngioma. *Neuro-oncology* (2018). doi:10.1093/neuonc/noy035
41. Dunn, I. F. *et al.* Mismatch Repair Deficiency in High-Grade Meningioma: A Rare but Recurrent Event Associated With Dramatic Immune Activation and Clinical Response to PD-1 Blockade. *JCO Precision Oncology* 1–12 (2018). doi:10.1200/PO.18.00190
42. Ke, R. *et al.* In situ sequencing for RNA analysis in preserved tissue and cells. *Nat. Methods* **10**, 857–860 (2013).
43. Krzywkowski, T. & Nilsson, M. Padlock Probes to Detect Single Nucleotide Polymorphisms. *Methods Mol. Biol.* **1649**, 209–229 (2018).
44. Krzywkowski, T., Hauling, T. & Nilsson, M. In Situ Single-Molecule RNA Genotyping Using Padlock Probes and Rolling Circle Amplification. *Methods Mol. Biol.* **1492**, 59–76 (2017).
45. Srivastava, S., Ghosh, S., Kagan, J. & Mazurchuk, R. The Making of a PreCancer Atlas: Promises, Challenges, and Opportunities. *Trends Cancer* **4**, 523–536 (2018).

46. Engel, K. B. & Moore, H. M. Effects of preanalytical variables on the detection of proteins by immunohistochemistry in formalin-fixed, paraffin-embedded tissue. *Arch. Pathol. Lab. Med.* **135**, 537–543 (2011).
47. Vassilakopoulou, M. *et al.* Preanalytical variables and phosphoepitope expression in FFPE tissue: quantitative epitope assessment after variable cold ischemic time. *Lab. Invest.* **95**, 334–341 (2015).
48. Masucci, G. V. *et al.* Validation of biomarkers to predict response to immunotherapy in cancer: Volume I - pre-analytical and analytical validation. *J Immunother Cancer* **4**, 76 (2016).
49. Swedlow, J. R., Goldberg, I., Brauner, E. & Sorger, P. K. Informatics and quantitative analysis in biological imaging. *Science* **300**, 100–102 (2003).
50. Goldberg, I. G. *et al.* The Open Microscopy Environment (OME) Data Model and XML file: open tools for informatics and quantitative analysis in biological imaging. *Genome Biol.* **6**, R47 (2005).
51. Moore, J. *et al.* Open tools for storage and management of quantitative image data. *Methods Cell Biol.* **85**, 555–570 (2008).
52. Schiffmann, D. A. *et al.* Open microscopy environment and findspots: integrating image informatics with quantitative multidimensional image analysis. *BioTechniques* **41**, 199–208 (2006).
53. Shen, D., Wu, G. & Suk, H.-I. Deep Learning in Medical Image Analysis. *Annu Rev Biomed Eng* **19**, 221–248 (2017).
54. Mika, S., Ratsch, G., Weston, J., Scholkopf, B. & Mullers, K. R. Fisher discriminant analysis with kernels. in *Neural Networks for Signal Processing IX: Proceedings of the 1999 IEEE Signal Processing Society Workshop (Cat. No.98TH8468)* 41–48 (1999). doi:10.1109/NNSP.1999.788121
55. THE USE OF MULTIPLE MEASUREMENTS IN TAXONOMIC PROBLEMS - FISHER - 1936 - Annals of Eugenics - Wiley Online Library. Available at: https://onlinelibrary.wiley.com/doi/abs/10.1111/j.1469-1809.1936.tb02137.x. (Accessed: 10th September 2018)

56. Schapiro, D. *et al.* Systematic analysis of cell phenotypes and cellular social networks in tissues using the histology topography cytometry analysis toolbox (histoCAT). (2017). doi:10.1101/109207
57. Simon, R. M., Paik, S. & Hayes, D. F. Use of archived specimens in evaluation of prognostic and predictive biomarkers. *J. Natl. Cancer Inst.* **101**, 1446–1452 (2009).
58. Mandrekar, S. J. & Sargent, D. J. Predictive biomarker validation in practice: lessons from real trials. *Clin Trials* **7**, 567–573 (2010).
59. Gosho, M., Nagashima, K. & Sato, Y. Study designs and statistical analyses for biomarker research. *Sensors (Basel)* **12**, 8966–8986 (2012).
60. Koch, B. *et al.* Generation and validation of homozygous fluorescent knock-in cells using CRISPR-Cas9 genome editing. *Nat Protoc* **13**, 1465–1487 (2018).
61. Lin, J.-R., Fallahi-Sichani, M. & Sorger, P. K. Highly multiplexed imaging of single cells using a high-throughput cyclic immunofluorescence method. *Nat Commun* **6**, 8390 (2015).
62. McKinley, E. T. *et al.* Optimized multiplex immunofluorescence single-cell analysis reveals tuft cell heterogeneity. *JCI Insight* **2**, (2017).
63. Grys, B. T. *et al.* Machine learning and computer vision approaches for phenotypic profiling. *J. Cell Biol.* **216**, 65–71 (2017).
64. Caicedo, J. C. *et al.* Data-analysis strategies for image-based cell profiling. *Nat. Methods* **14**, 849–863 (2017).
65. Espina, V. *et al.* Tissue is alive: New technologies are needed to address the problems of protein biomarker pre-analytical variability. *Proteomics Clin Appl* **3**, 874–882 (2009).
66. Hicks, D. G. & Boyce, B. F. The challenge and importance of standardizing pre-analytical variables in surgical pathology specimens for clinical care and translational research. *Biotech Histochem* **87**, 14–17 (2012).

67. References. in *Finite Mixture Models* 349–393 (Wiley-Blackwell, 2005). doi:10.1002/0471721182.refs
68. Wilks, S. S. The Large-Sample Distribution of the Likelihood Ratio for Testing Composite Hypotheses. *Ann. Math. Statist.* **9**, 60–62 (1938).
69. Schwarz, G. Estimating the Dimension of a Model. *Ann. Statist.* **6**, 461–464 (1978).
70. Amir, E. D. *et al.* viSNE enables visualization of high dimensional single-cell data and reveals phenotypic heterogeneity of leukemia. *Nat. Biotechnol.* **31**, 545–552 (2013).
71. Samusik, N., Good, Z., Spitzer, M. H., Davis, K. L. & Nolan, G. P. Automated mapping of phenotype space with single-cell data. *Nat. Methods* **13**, 493–496 (2016).
72. Wang, C., Hillsamer, P. & Kim, C. H. Phenotype, effector function, and tissue localization of PD-1-expressing human follicular helper T cell subsets. *BMC Immunol.* **12**, 53 (2011).
73. Uhlen, M. *et al.* A proposal for validation of antibodies. *Nat. Methods* **13**, 823–827 (2016).
74. Dove, A., 2017 & Pm, 2:00. Agreeable antibodies: Antibody validation challenges and solutions. *Science | AAAS* (2017). Available at: http://www.sciencemag.org/features/2017/09/agreeable-antibodies-antibody-validation-challenges-and-solutions. (Accessed: 15th July 2018)
75. Roncador, G. *et al.* The European antibody network's practical guide to finding and validating suitable antibodies for research. *MAbs* **8**, 27–36 (2016).
76. Ellington, A. A., Kullo, I. J., Bailey, K. R. & Klee, G. G. Antibody-based protein multiplex platforms: technical and operational challenges. *Clin. Chem.* **56**, 186–193 (2010).
77. Wang, W., Lilyestrom, W. G., Hu, Z. Y. & Scherer, T. M. Cluster Size and Quinary Structure Determine the Rheological Effects of Antibody Self-Association at High Concentrations. *J Phys Chem B* **122**, 2138–2154 (2018).
78. Herring, C. A. *et al.* Unsupervised Trajectory Analysis of Single-Cell RNA-Seq and Imaging Data Reveals Alternative Tuft Cell Origins in the Gut. *Cell Syst* **6**, 37-51.e9 (2018).

79. Gulshan, V. *et al.* Development and Validation of a Deep Learning Algorithm for Detection of Diabetic Retinopathy in Retinal Fundus Photographs. *JAMA* **316**, 2402–2410 (2016).
80. Churlaud, G. *et al.* Human and Mouse CD8(+)CD25(+)FOXP3(+) Regulatory T Cells at Steady State and during Interleukin-2 Therapy. *Front Immunol* **6**, 171 (2015).
81. Kiniwa, Y. *et al.* CD8+ Foxp3+ regulatory T cells mediate immunosuppression in prostate cancer. *Clin. Cancer Res.* **13**, 6947–6958 (2007).
82. Yang, Z.-Q. *et al.* Increased liver-infiltrating CD8+FoxP3+ regulatory T cells are associated with tumor stage in hepatocellular carcinoma patients. *Hum. Immunol.* **71**, 1180–1186 (2010).
83. Woo, S.-R. *et al.* Immune inhibitory molecules LAG-3 and PD-1 synergistically regulate T-cell function to promote tumoral immune escape. *Cancer Res.* **72**, 917–927 (2012).
84. Bottai, G. *et al.* An immune stratification reveals a subset of PD-1/LAG-3 double-positive triple-negative breast cancers. *Breast Cancer Res.* **18**, 121 (2016).
85. Matsuzaki, J. *et al.* Tumor-infiltrating NY-ESO-1-specific CD8+ T cells are negatively regulated by LAG-3 and PD-1 in human ovarian cancer. *Proc. Natl. Acad. Sci. U.S.A.* **107**, 7875–7880 (2010).
86. Banerjee, A., McKinley, E. T., von Moltke, J., Coffey, R. J. & Lau, K. S. Interpreting heterogeneity in intestinal tuft cell structure and function. *J. Clin. Invest.* **128**, 1711–1719 (2018).

TABLES

Table 1. t-CyCIF staining plan for immune profile panel.

	488/FITC					555/Cy3					647/Cy5				
Cycle	Name	Clone	Vendor	Cat #	Dil	Name	Clone	Vendor	Cat #	Dil	Name	Clone	Vendor	Cat #	Dil
0						**Goat anti-Rabbit**		Thermo Fisher	A-21428	1000	**Goat anti-Mouse**		Thermo Fisher	A-21235	1000
1						**LAG3**	EPR4392(2)	Abcam	ab180187	100					
2	**Ki-67**	D3B5	CST	11882s	100	**Keratin**	AE1/AE3	eBioscience	41-9003-80	200	**PD-1**	EPR4877(2)	Abcam	ab201825	100
3	**CD45RB**	PD7/26	eBioscience	53-9458-80	100	**CD3**	EP4426	Abcam	ab208514	100	**PD-L1**	E1L3N	CST	15005S	50
4	**CD4**	Polyclonal	R&D Systems	FAB8165G	100	**CD45**	2D1	R&D Systems	FAB1430P-025	100	**CD8a**	AMC908	eBioscience	50-0008-80	100
5	**CD163**	EPR14643	Abcam	ab218293	100	**CD68**	D4B9C	CST	#79594	100	**CD14**	EPR3653	Abcam	ab196169	100
6	**CD11b**	C67F154	eBioscience	53-0196-80	100	**Foxp3**	236A/E7	eBioscience	41-4777-80	100					
7	**IBA1**	EPR6136	Abcam	ab195031	250	α-SMA	EPR5368	Abcam	ab202509	250	**CD20**	L26	eBioscience	50-0202-80	250
8	**CD19**	EPR5906	Abcam	ab196468	100	**GFAP**	GA5	eBioscience	41-9892-80	100					

1 **Table 2 | Troubleshooting table.**

Step	Problem	Possible reason	Solution
5	Leica BOND RX machine fails to start	Incorrect setup of Leica BOND RX machine	Read the manufacturer's instructions; check the protocol and reagent setup carefully; contact vendor
6	No bubbles in fluorophore bleaching solution	Incorrect lighting source or bleaching solution used	Use white LED light for fluorophore inactivation; use freshly made bleaching solution
13, 22, 35	Blurry images	The slides are not flat and focusing is suboptimal	Examine the slide holder for precipitate and remove; ensure that slides are loaded properly in the slide holder; change coverslips; adjust the focusing points
22, 35	Weak signal	Low signal can result because of low level antigen expression. Direct immunofluorescence using conjugated antibodies does not provide the signal amplification that can be generated in indirect immunofluorescence	Increase the exposure time while acquiring image; increase the antibody concentration during staining step; use the corresponding unconjugated antibodies in the first round instead of the conjugated antibody to see if signal amplification from indirect immunofluorescence improves signal; if necessary, find an alternative antibody
22, 35	Saturated signal	Abundant antigen in sample or excessive amount of antibody	Decrease the antibody concentration used during the staining steps; decrease the incubation time of the sample with antibody;

			decrease the exposure time during image acquisition
35	Cell loss	Tissue type (very low cell density), tissue fixation (insufficient fixation), t-CyCIF performance (rough handling of samples; e.g. washing)	Cautious handling of samples during application of antibodies and washing steps as well as during manipulation of coverslips
35	Signal present after fluorophore bleaching step	Insufficient fluorophore inactivation	Avoid Alexa Fluor–546, Alexa Fluor–568, and Alexa Fluor–594 conjugated antibodies, because they are difficult to be inactivate; dilute conjugated antibodies further; extend fluorophore bleaching time; increase H_2O_2 concentration from 3% to 4.5%

1

FIGURE LEGENDS

Figure 1 | Schematic of antibody validation approaches for multiplexed tissue imaging. The displayed approaches are the cornerstones for validating antibodies for use in any of the several emerging multiplex imaging methods. Validation approaches are described at the a. pixel level, b. cell level, and c. tissue level. Each of these approaches is discussed in detail in the text. The t-CyCIF protocol is used in this manuscript to illustrate how antibody validation, spatially resolved immune cell cataloging, and rare cell identification can be achieved via a multiplexing technology. The t-CyCIF method[9] has three major parts: bench work (Steps 1-35), image processing (Steps 36-38), and high dimension data analysis and data visualization (Steps 39-45). Antibodies can be compared to each other at the level of pixels, cells or tissues.

Figure 2 | Pixel-by-Pixel validation of antibodies raised against PD-1 using t-CyCIF in human tonsil. a. Representative images of immunofluorescence staining from human FFPE tonsil sections using four different PD-1 antibodies: PD-1 (EPR4877, Abcam), PD-1 (NAT105, Abcam), PD-1 (EH33, CST) and PD-1 (D4W2J, CST); **b**. Plots of the pixel-by-pixel correlation of the signal intensity of four PD-1 antibodies were generated. The plots display the correlation of a random sampling of 2,000 pixels. The plots on the lower left (with blue dots) are of the original fluorescence intensity at each pixel and the plots on the upper right (with cyan dots) are of the log transformed fluorescence intensity at each pixel. The Pearson correlation coefficients (R) are shown. DR: Dynamic range.

Figure 3 | Validation of antibodies for immune profiling by comparison to clinical grade antibodies. Representative images of t-CyCIF and IHC are shown for **a.** CD3, **b.** CD20, **c.** CD4 and **d.** PD-1 in human FFPE tonsil sections. **e.** and **f.** Correlation plots comparing the percentage of positive cells detected by t-CyCIF and by IHC staining for each immune marker antibody. Positive cells from the t-CyCIF data were identified using either **e.** manual gating or **f.** Gaussian mixture model analysis, and thresholds for indicating positive cells for IHC were set using Aperio ImageScope software.

Figure 4 | Validation of antibodies for immune profiling by co-segregation of known markers and expected spatial localization. a. Representative images of CD3, CD4, IBA1, CD8a, FOXP3, PD-1 and PD-L1 as well as **b. – e.** merged images from human tonsil are presented. A compilation of images for all other immune markers is available in **Supplementary**

Movie 1 and **Supplementary Figure 9-10**. Scatter plots were created from a random sampling of data from 10,000 cells. Both manual gating (black dashed lines) and Gaussian mixture model analysis (red ovals) highlight positive and negative cell populations.

Figure 5 | Spatially resolved cataloging of immune cells in lung cancer FFPE tissue and component analysis of the immune subpopulations by t-CyCIF. a. Montage of t-CyCIF immunofluorescence staining for four antigens in primary lung cancer resection sample (LUNG-3-PR): α-SMA (green) for stromal myofibroblastic cells, pan-keratin (blue) for tumor cells, and CD45 or IBA1 (red) for immune cells. **b.** Corresponding map of cell position in which the intensity of the immunofluorescence data was integrated over each entire cell, with dots representing the computed centroid for each cell and the colors representing the identify of each of the cells: α-SMA+ stromal myofibroblasts (green), pan-keratin+ tumor cells (blue), and CD45+ or IBA1+ immune cells (red). The values of the x and y axes are in millimeters (mm). 2D-spatially resolved intensity maps (red high; blue low) showing the relative levels of expression of **c.** pan-keratin and **d.** PD-L1. **e.** A representative merged image of pan-keratin (green), Ki-67 (white) and PD-L1 (red) immunofluorescence from frame 55 (yellow box in **a.-d.**) as well as **f.** a representative image from the H&E stain from a similar region from the next adjacent serial section of LUNG-3-PR. **g.** t-SNE plots for immune cell markers CD45, CD3, CD20, CD163 and CD11b from a random sampling of 2,000 immune cells from lung cancer samples LUNG-1-LN, LUNG-2-BR and LUNG-3-PR. The upper left panel shows the discrete clustering of the immune populations from each case. The additional panels show the intensity of staining for the indicated markers which is mapped to color (red - high; blue - low). **h.** Bar graph showing the percentage of each immune cell type relative to the total number of immune cells in the lung cancer samples (see **Supplementary Table 7** for quantified data).

Figure 6 | Illustration of low frequency CD45+/CD3+/FOXP3+/CD4-/CD8a+ T cells detected and confirmed by t-CyCIF. Scatter plots of CD4 and FOXP3 expression in lung cancer sample LUNG-3-PR with **a.** CD3 and **b.** CD8a expression mapped to color (red - high; blue – low). 6.08% of the immune cells were CD45+/CD3+/FOXP3+/CD4+/CD8a-, while 0.66% of the immune cells were CD45+/CD3+/FOXP3+/CD4-/CD8a+ (see **Supplementary Table 8** for additional details). **c**. 2D-dot plot map of the spatial distribution of CD45+/CD3+/FOXP3+/CD4+/CD8a- cells (green dots) and CD45+/CD3+/FOXP3+/CD4-

/CD8a+ cells (red dots) in lung cancer sample LUNG-3-PR. We found four CD45+/CD3+/FOXP3+/CD4-/CD8a+ cells (red dots) in frame 55 of this lung cancer sample and confirmed the presence of these four cells (red rectangles) by **d.** visual review of the t-CyCIF data. Bar graph of **e.** regional enrichment analysis and of **f.** manual counting of t-CyCIF data showing that CD45+/CD3+/FOXP3+/CD4+/CD8a- cells and CD45+/CD3+/FOXP3+/CD4-/CD8a+ cells were significantly enriched in the tumor region compared to the non-tumor region (see **Supplementary Table 9** for additional details). Error bars represent standard error of the mean (SEM). *, $p < 0.05$; **, $p < 0.01$; ***, $p < 0.001$; ****, $p < 0.0001$, t-test

Figure 7 | Illustration of low frequency CD45+/CD3+/PD-1+/LAG3+ T cells detected and confirmed by t-CyCIF. Scatter plots of LAG3 and PD-1 expression in lung cancer sample LUNG-3-PR with **a.** CD3, **b.** CD8a, and **c.** CD4 expression mapped to color (red - high; blue – low). 2.49% of the immune cells were CD45+/CD3+/PD-1+, 1.21% of the immune cells were CD45+/CD3+/PD-1+/LAG3+, 0.97% of the immune cells were CD45+/CD3+/PD-1+/LAG3+/CD4-/CD8a+ and 0.08% of immune cells were CD45+/CD3+/PD-1+/LAG3+/CD4+/CD8a- (see **Supplementary Table 8** for more details). **d**. 2D-dot plot map of the spatial distribution of CD45+/CD3+/PD-1+/LAG3+/CD4-/CD8a+ cells (green dots) and CD45+/CD3+/ PD-1+/LAG3+/CD4+/CD8a- cells (red dots) in lung cancer sample LUNG-3-PR. We found one CD45+/CD3+/PD-1+/LAG3+/CD4+/CD8a- cell (red dot) and two CD45+/CD3+/PD-1+/LAG3+/CD4-/CD8a+ cells (green dots) in frame 55 of lung cancer sample LUNG-3-PR and **g.** confirmed the presence of these T cell subpopulations by visual review of the t-CyCIF data with the two different cell subpopulations indicated by red and green rectangles, respectively). Bar graph of **e.** regional enrichment analysis and of **f.** manual counting of t-CyCIF data showing that CD45+/CD3+/PD-1+/LAG3+/CD4+/CD8a- cells and CD45+/CD3+/PD-1+/LAG3+/CD4-/CD8a+ cells were significantly enriched in the tumor region compared to the non-tumor region (see **Supplementary Table 9** for additional details). Scale bars are indicated in the images and their insets. Error bars represent standard error of the mean (SEM). *, $p < 0.05$; **, $p < 0.01$; ***, $p < 0.001$; ****, $p < 0.0001$, t-test

Figure 8 | Systematic identification of rare subpopulations using the t-CyCIF method. a. All PD-1+ cells (n=273) from the LUNG-2-PR (match with results) sample were further separated using binary gating of all 15 different immune markers. The subpopulations

comprising 3 or more cells were listed. Highlighted with yellow is the subpopulation with PD-1+/LAG3+/CD8a+/CD3+ (described by visual review of scatter plots in Figure 8. **b.** Gallery of images of single markers from single cells from the PD-1+/LAG3+/CD8a+/CD3+ subpopulation.

SUPPLEMENTARY MATERIALS

Supplementary Movie 1 | t-CyCIF images from FFPE human tonsil tissue.

Supplementary Movie 2 | t-CyCIF images from a FFPE human primary lung cancer resection sample – LUNG-3-PR.

Supplementary Table 1 | t-CyCIF immune profile antibody panel.

Supplementary Table 2 | Dynamic range and Pearson's r of the dynamic range between antibodies.

Supplementary Table 3 | Antibody information for the immune t-CyCIF panel.

Supplementary Table 4 | Clinical antibodies used for immunohistochemistry validation.

Supplementary Table 5 | Antigenicity with cycle number in t-CyCIF.

Supplementary Table 6 | Correlation in staining intensity between early and late cycles.

Supplementary Table 7 | The percentage of tumor cells, fibroblasts and immune cells (percentage to all cells) in lung cancer cases.

Supplementary Table 8 | The immune profile (ratio to all immune cells) in lung cancer cases.

Supplementary Table 9 | Regional enrichment analysis (percentage to all immune cells) of rare immune cells in lung cancer cases.

Supplementary Figure 1 | Markers and major cell types identified by t-CyCIF immune panel. a. Canonical immune cell types and their markers. Seven major immune cell subtypes were assayed using a panel of 16 markers. Three additional markers (Ki-67, α-SMA and pan-Keratin) were used to identified cell states (Ki-67 for proliferative cells) or to separate immune cells from tumor cells (Keratin positive) or stromal cells (alpha SMA positive). **b.** Actual immune subpopulation identified from t-CyCIF immune profiling of a primary lung adenocarcinoma (LUNG-2-BR). A total 23,079 immune cells (keratin/α-SMA negative cells) from the sample was used for binary gating of 15 different markers. A total 1,356 different subpopulations were identified of which 37 subpopulations represented over 0.5 percent of total immune cells. The four subpopulations that were highlighted here are CD45+/IBA1+(Macrophage or Dendritic cells), CD45+/CD20+ (B cells), CD45+/CD3+/CD8a+ (Cytotoxic T cells) and CD45+/CD3+/CD4+ (T helper cells). Asterisks label 19 common immune cell subtypes.

Supplementary Figure 2 | Evaluation of segmentation accuracy and error composition. a. Overall error rates of segmentation. Several hundred segmented masks were validated by human review and the errors versus total counts of segmented cells from four different samples (Tonsil, LUNG-1-LN, LUNG-2-BR and LUNG-3-PR) were plotted. The average error rate was ~20% (S.E. 2%) for each of the samples. **b**. Illustration of the types of errors encountered. An example single-channel gray-scale Hoechst image is shown including the segmented masks that were highlighted in yellow. Three major types of segmentation errors were found: fused (blue arrows), split (red arrows) and missed (green arrows) cells. **c.** The composition of the different types of segmentation errors from the four different samples.

Supplementary Figure 3 | Illustration of manual inspection and gating of intensity data. a. Histogram of single-cell intensity from CD8a staining. Human-inspection of this signal profile was used to set the gate/threshold at 8.5 log. The digital representation of the same intensity data was projected into physical maps of **b.** the original intensity data in log scale, **c.** data with all positive cells colored in red and **d.** the relative density of positive cells.

Supplementary Figure 4 | Multi-antibody qualification of PD-L1 and FOXP3 antibodies by t-CyCIF in human FFPE tonsil tissue. Representative images of immunofluorescence staining from human FFPE tonsil sections using **a.** three different antibodies for PD-L1: PD-L1 AB1

(E1L3N, CST), PD-L1 AB2 (22C3, DAKO), and PD-L1 AB3 (28-8, Abcam). **c.** two different antibodies for FOXP3: FOXP3 AB1 (23A/E7, eBioscience) and FOXP3 AB2 (206D, BioLegend). Plots of the pixel-by-pixel correlation of the signal intensity generated by the **b.** PD-L1 antibodies and **d.** FOXP3 antibodies. The plots display the correlation of a random sampling of 2,000 pixels. The plots on the lower left (with blue dots) are of the original fluorescence intensity at each pixel and the plots on the upper right (with cyan dots) are of the log transformed fluorescence intensity at each pixel. The Pearson correlation coefficients (r) are shown. DR: Dynamic range.

Supplementary Figure 5 │ Multi-antibody qualification of CD45 antibodies by t-CyCIF in human FFPE tonsil tissue. Individual and merged **a.** low and **b.** high magnification images of immunofluorescence from three CD45 antibodies: CD45 AB1 (2D1, R&D), CD45 AB2 (HI30, BioLegend), and CD45RB AB3 (PD7/26, eBioscience). **c.** Plots of the pixel-by-pixel correlation of the signal intensity generated by the CD45 antibodies. The plots display the correlation of a random sampling of 2,000 pixels. The plots on the lower left (with blue dots) are of the original fluorescence intensity at each pixel and the plots on the upper right (with cyan dots) are of the log transformed fluorescence intensity at each pixel. DR: Dynamic range.

Supplementary Figure 6 │ Multi-antibody qualification of LAG3 antibodies by t-CyCIF in human FFPE tonsil tissue. Individual and merged **a.** low and **b.** high magnification images of immunofluorescence from five LAG3 antibodies: LAG3 AB1 (EPR4392, Abcam), LAG3 AB2 (Polyclonal, R&D), LAG3 AB3 (17B4, Lifespan), LAG3 AB4 (11E3, Abcam) and LAG3 AB5 (T47-530, BD Bioscience). **c.** Plots of the pixel-by-pixel correlation of the signal intensity generated by the LAG3 antibodies. The plots display the correlation of a random sampling of 2,000 pixels. The plots on the lower left (with blue dots) are of the original fluorescence intensity at each pixel and the plots on the upper right (with cyan dots) are of the log transformed fluorescence intensity at each pixel. DR: Dynamic range

Supplementary Figure 7 │ Multi-antibody qualification of CD11b antibodies by t-CyCIF in human FFPE tonsil tissue. Individual and merged **a.** low and **b.** high magnification images of immunofluorescence from three CD11b antibodies: CD11b AB1 (EP1345Y, Abcam), CD11b AB2 (C67F154, c), and CD11b AB3 (EPR1344, Abcam). **c.** Plots of the pixel-by-pixel correlation of the signal intensity generated by the CD11b antibodies. The plots display the

correlation of a random sampling of 2,000 pixels. The plots on the lower left (with blue dots) are of the original fluorescence intensity at each pixel and the plots on the upper right (with cyan dots) are of the log transformed fluorescence intensity at each pixel. DR: Dynamic range

Supplementary Figure 8 | Multi-antibody qualification by t-CyCIF and IHC in human FFPE tonsil tissue. Representative images of t-CyCIF and IHC staining using antibodies to **a.** CD8a, **b.** FOXP3, **c.** PD-L1, **d.** CD68, **e.** Bar plot of the percentage of total immune cells in the tonsil section that were positive for the specified antibodies. The estimated number of positive cells was determined by both manual gating and by Gaussian mixture model analysis. The plot includes the percentage of positive cells for each immune antibody by IHC; counted using Aperio ImageScope software, Leica, USA.

Supplementary Figure 9 | Immune profiling in human FFPE tonsil tissue by t-CyCIF. Merged images of t-CyCIF data from frame 106 of and scatter plots from a random sampling of 10,000 cells for **a**. CD3 and CD45RB, **b.** CD3 and FOXP3, **c.** LAG3 and PD-1, **d.** IBA1 and CD16. **e**. Additional merged images from Frame 106 for CD3 and CD20, CD4 and CD8a, CD19 and CD20, CD11b and CD14, CD163 and CD68, and IBA1 and CD14.

Supplementary Figure 10 | Individual t-CyCIF images for 16 different immune markers in human FFPE tonsil tissue (frame 106).

Supplementary Figure 11 | Analysis of effect of t-CyCIF cycle number on antigenicity with in human FFPE tonsil tissue. Histograms of signal intensity and representative images of t-CyCIF from eight sequential sections of human FFPE tonsil tissue across different staining cycles for **a.** CD3, **b.** CD4, **c.** CD8a, **d.** CD20, and **e.** FOXP3. The same antibody concentration and the same exposure time for imaging was used in the different cycles (see **Supplementary Table 5, 6** for additional details). The histogram plots were made from single cell data to show the intensity distribution from the different populations from different cycles. For the representative t-CyCIF images shown, the same threshold was used for each marker for visualization and comparison. In **e.** the black arrow indicates the FOXP3+ population.

Supplementary Figure 12 | Analysis of effect of t-CyCIF cycle number on antigenicity with in human FFPE tonsil tissue. Histograms of signal intensity and representative images of t-CyCIF from eight sequential sections of human FFPE tonsil tissue across different staining

cycles for **a.** IBA1, **b.** CD14, **c.** CD68, **d.** CD163, and **e.** Keratin. The same antibody concentration and the same exposure time for imaging was used in the different cycles (see **Supplementary Table 5, 6** for additional details). The histogram plots were made from single cell data to show the intensity distribution from the different populations from different cycles. For the representative t-CyCIF images shown, the same threshold was used for each marker for visualization and comparison. In **e.** the black arrow indicates the Keratin+ population.

Supplementary Figure 13 | H&E images of lung cancer specimens. Whole slide scans of H&E stained slides of **a.** lung adenocarcinoma metastasis to lymph node (LUNG-1-LN), **b.** lung squamous cell carcinoma metastasis to brain (LUNG-2-BR), and **c.** primary lung squamous cell carcinoma (LUNG-3-PR).

Supplementary Figure 14 | Geographic visualization of t-CyCIF data in cancer samples LUNG-1-LN and LUNG-2-BR. a. Montage of t-CyCIF images and **b.** corresponding dot plot for tumor cells (Keratin+, blue), fibroblasts (α-SMA+, green) and immune cells (CD45+ or IBA1+, red) in lung cancer sample LUNG-1-LN. **c** Representative merged images of t-CyCIF data for α-SMA, Keratin, CD45RB and IBA1, CD20, CD3 from lung cancer sample LUNG-1-LN (frame 36). **d.** Montage of t-CyCIF images and **e.** corresponding dot plot for tumor cells (Keratin+, blue), fibroblasts (α-SMA+, green) and immune cells (CD45+ or IBA1+, red) in lung cancer sample LUNG-2-BR. **f.** Representative merged images of t-CyCIF data for α-SMA, Keratin, CD45RB and IBA1, CD20, CD3 from lung cancer sample LUNG-2-BR (frame 137).

Supplementary Figure 15 | t-SNE analysis of immune cells from lung cancer samples. t-SNE plots of immune cell markers CD4, CD8a, FOXP3, IBA1, CD68, CD14, PD-1, PD-L1 and LAG3 from a random sampling of 2,000 immune cells for lung cancer samples LUNG-1-LN, LUNG-2-BR and LUNG-3-PR. The staining for each of the indicated markers is mapped to color (red - high; blue - low).

Supplementary Figure 16 | Low frequency immune cell types detected and confirmed by t-CyCIF in lung cancer samples LUNG-1-LN and LUNG-2-BR by t-CyCIF. a. Scatter plots of CD4 and FOXP3 expression in lung cancer sample LUNG-1-LN with CD3 and CD8a expression mapped to color (red - high; blue – low). 2.31% of the immune cells were CD45+/CD3+/FOXP3+/CD4+/CD8a- while 0.031% of the immune cells were

CD45+/CD3+/FOXP3+/CD4-/CD8a+ (see **Supplementary Table 8** for additional details). **b.** Representative image of t-CyCIF data for CD4, CD8a and FOXP3 (LUNG-1-LN, frame 36). **c.** Scatter plot for CD4 and FOXP3, with CD3 and CD8a mapped to color (red – high, blue – low) in lung cancer sample LUNG-2-BR. 2.65% of the immune cells were CD45+/CD3+/FOXP3+/CD4+/CD8a- while 0.006% cells of the immune cells were CD45+/CD3+/FOXP3+/CD4-/CD8a+ (see **Supplementary Table 8** for additional details). **d.** Merged image of t-CyCIF data for CD4, CD8a and FOXP3 (LUNG-2-BR, frame 137. **e.** Scatter plots for LAG3 and PD-1expression in lung cancer sample LUNG-1-LN with CD3 and CD8a expression mapped to color (red - high; blue – low). 3.6% of the immune cells were CD45+/CD3+/PD-1+ while 0.87% of the immune cells were CD45+/CD3+/PD-1+/LAG3+ cells, 0.67% cells were CD45+/CD3+/ PD-1+/LAG3+/ CD4-/CD8a+ and 0.07% were CD45+/CD3+/PD-1+/LAG3+/ CD4+/CD8a- (see **Supplementary Table 8** for additional details).

Supplementary Figure 17 │ Images from nine rare subtypes of PD-1 expressing cells. Coordinates of a selected cell subpopulation (CD45+/CD3+/CD8a+/PD-1+/LAG3+ cells) were used to extracted single-cell images from t-CyCIF imaging data from the LUNG-2-BR sample. The 15 individual channels of images from ten different cells (including the one shown in Figure 9) were displayed in 40µm x 40µm grids, with the cell of interest centered in each grid. The highlighted channels (LAG3, PD-1, CD3, CD45 and CD8a) were positive in all ten cells.

Figure-1 (Santagata)

Approaches to Antibody Testing and Qualification

a. Pixel Level

Images (Same specimen)

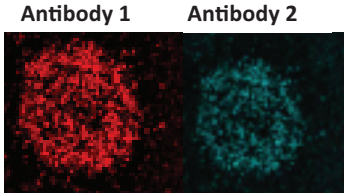

Pixel by pixel correlation

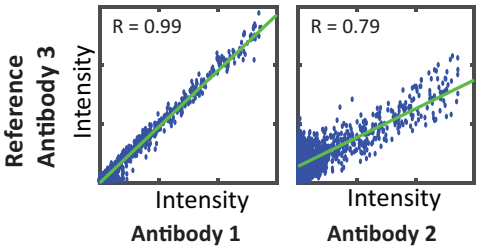

b. Cell Level

Image Segmentation

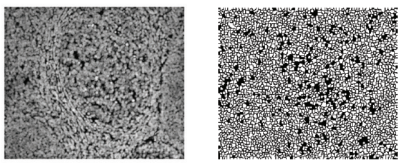

CyCIF data with manual gating

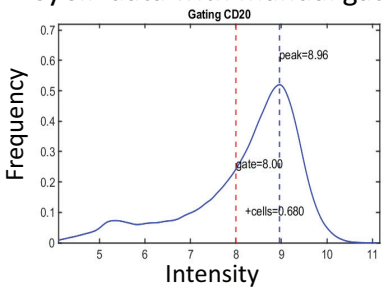

CyCIF data with GMM gating

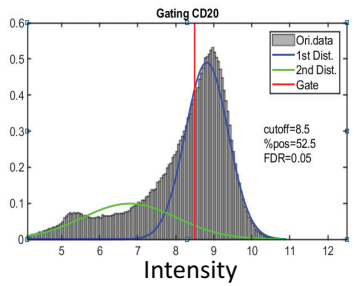

Co-Segregation of Markers

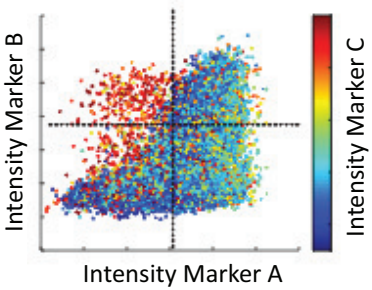

Comparison of Fluoresence Images to IHC of Clinical Grade Antibodies

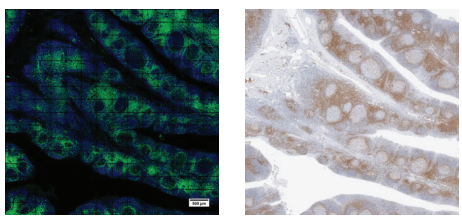

Multidimensional Clustering of Cell State Vectors

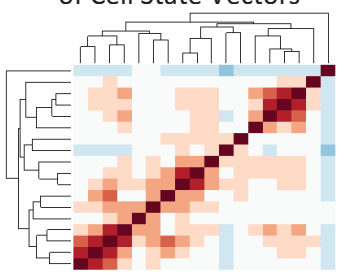

c. Tissue Level

Spatial Distribution In Well-characteized Tissues

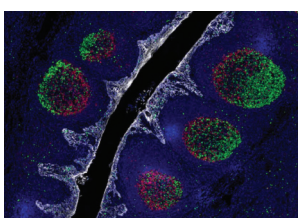

Figure-2 (Santagata)

a

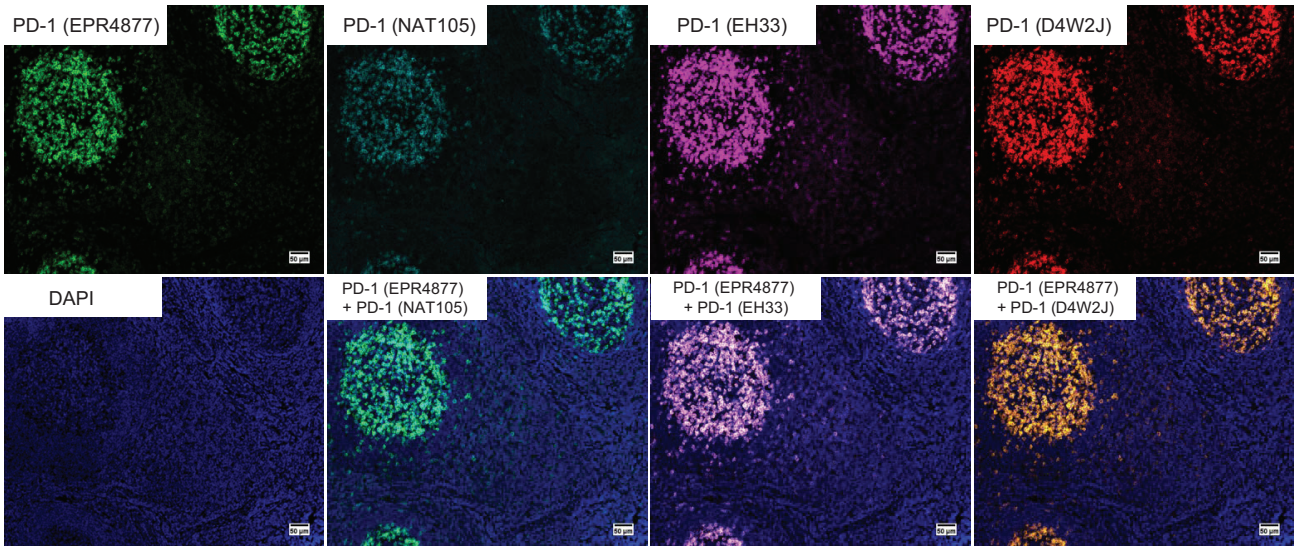

b

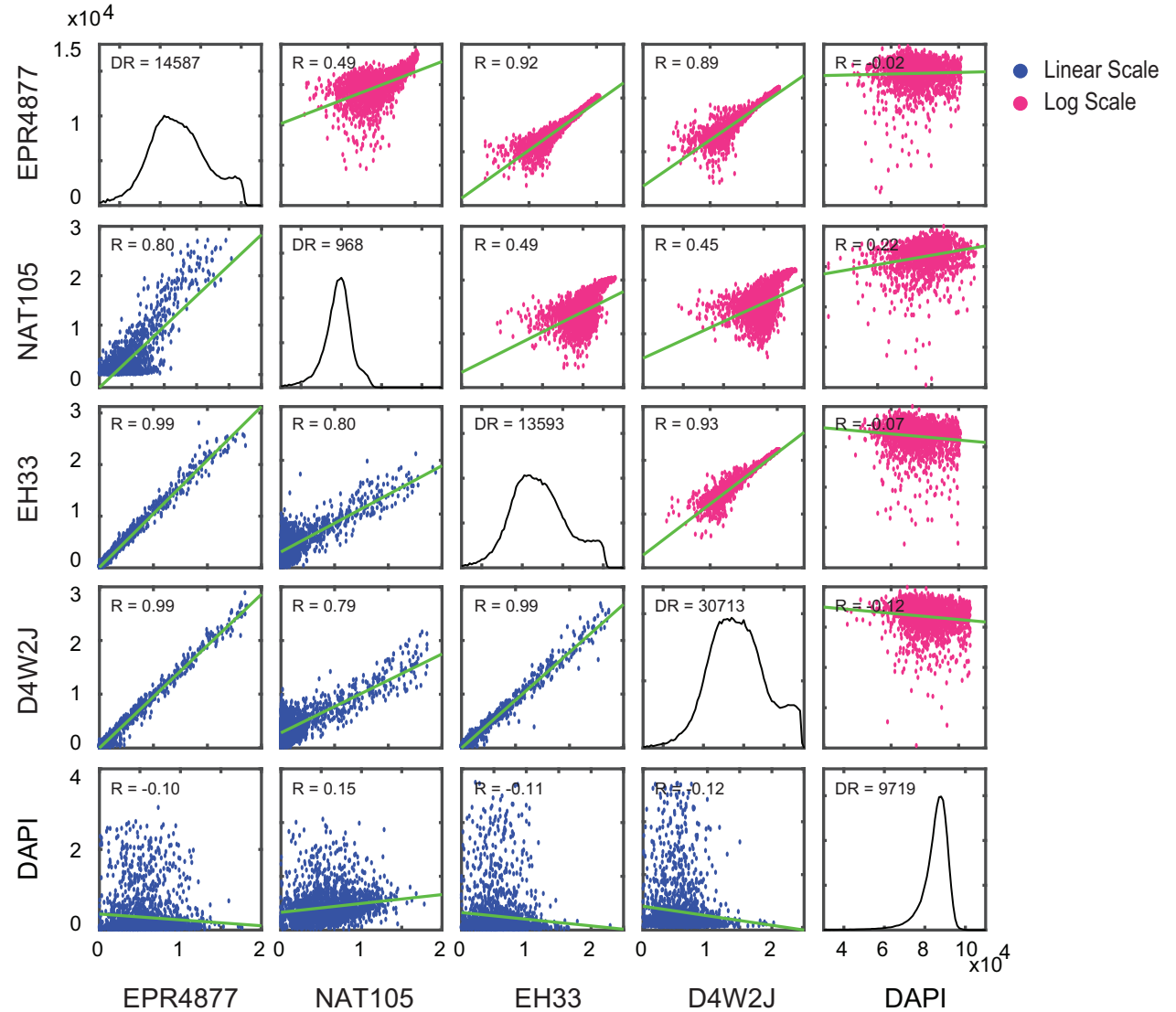

Figure-3 (Santagata)

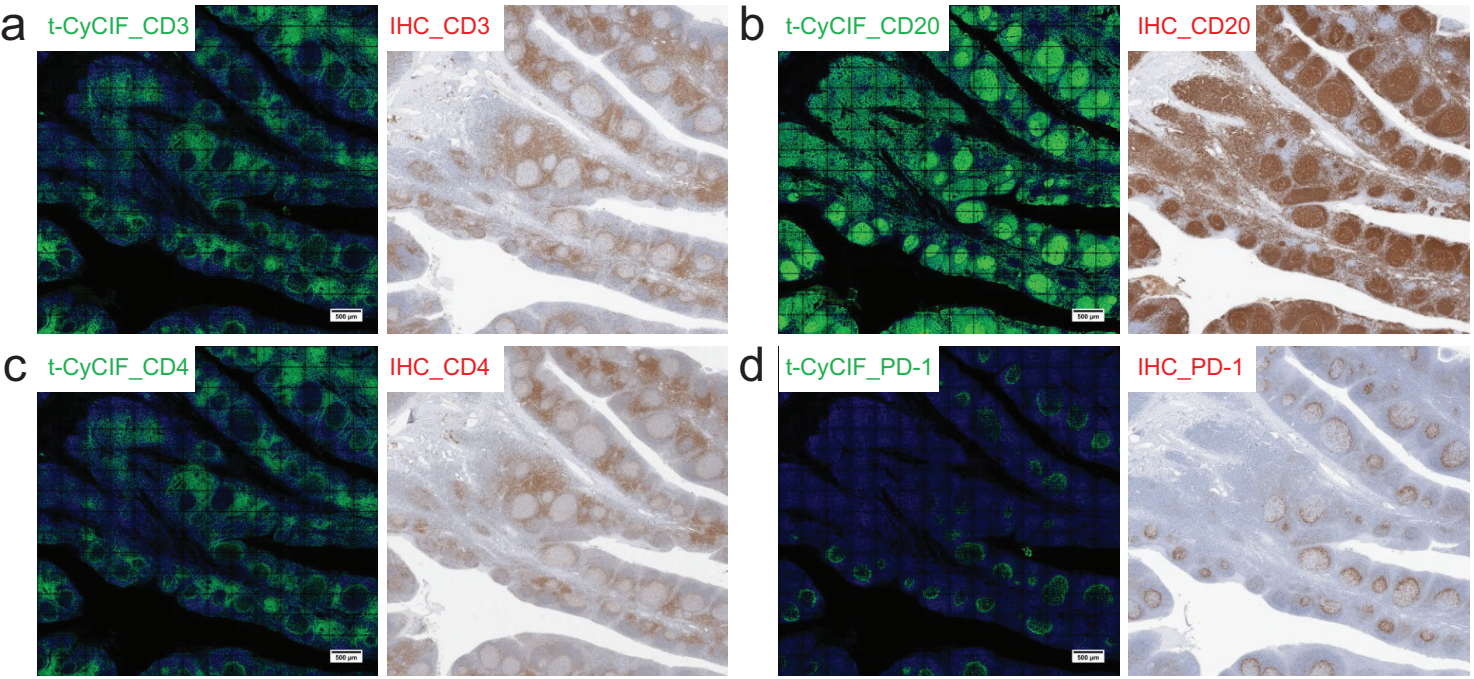

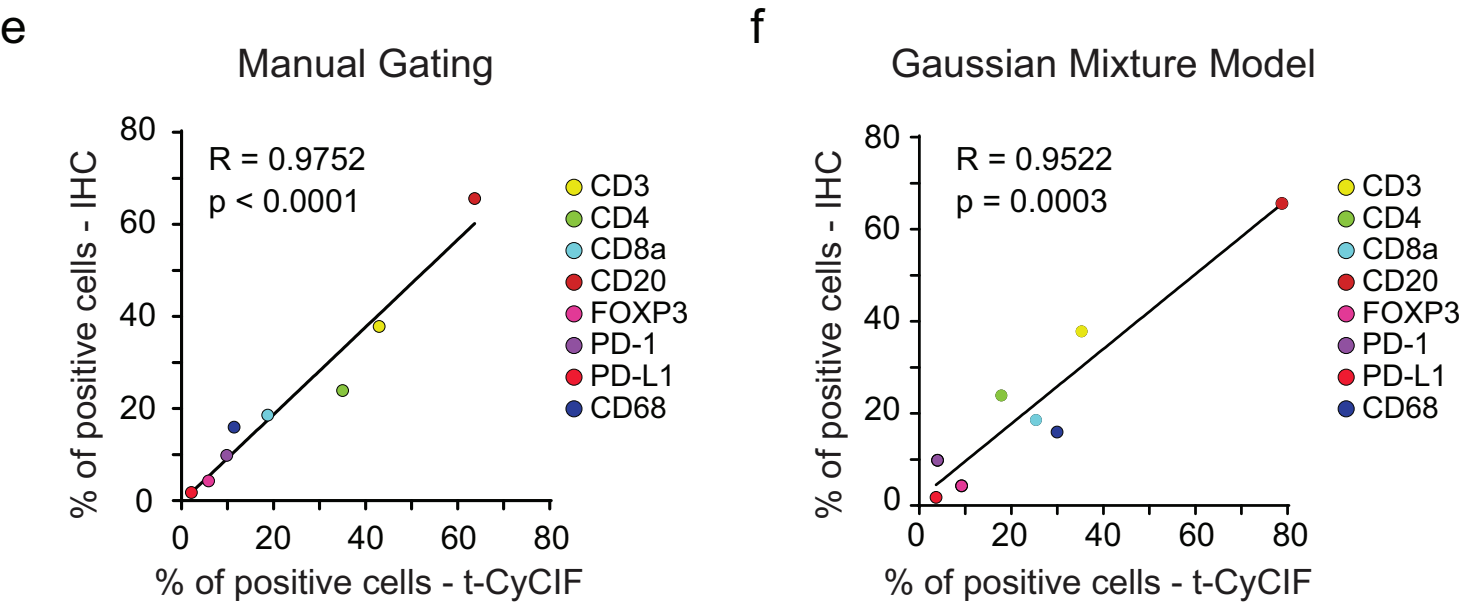

Figure-4 (Santagata)

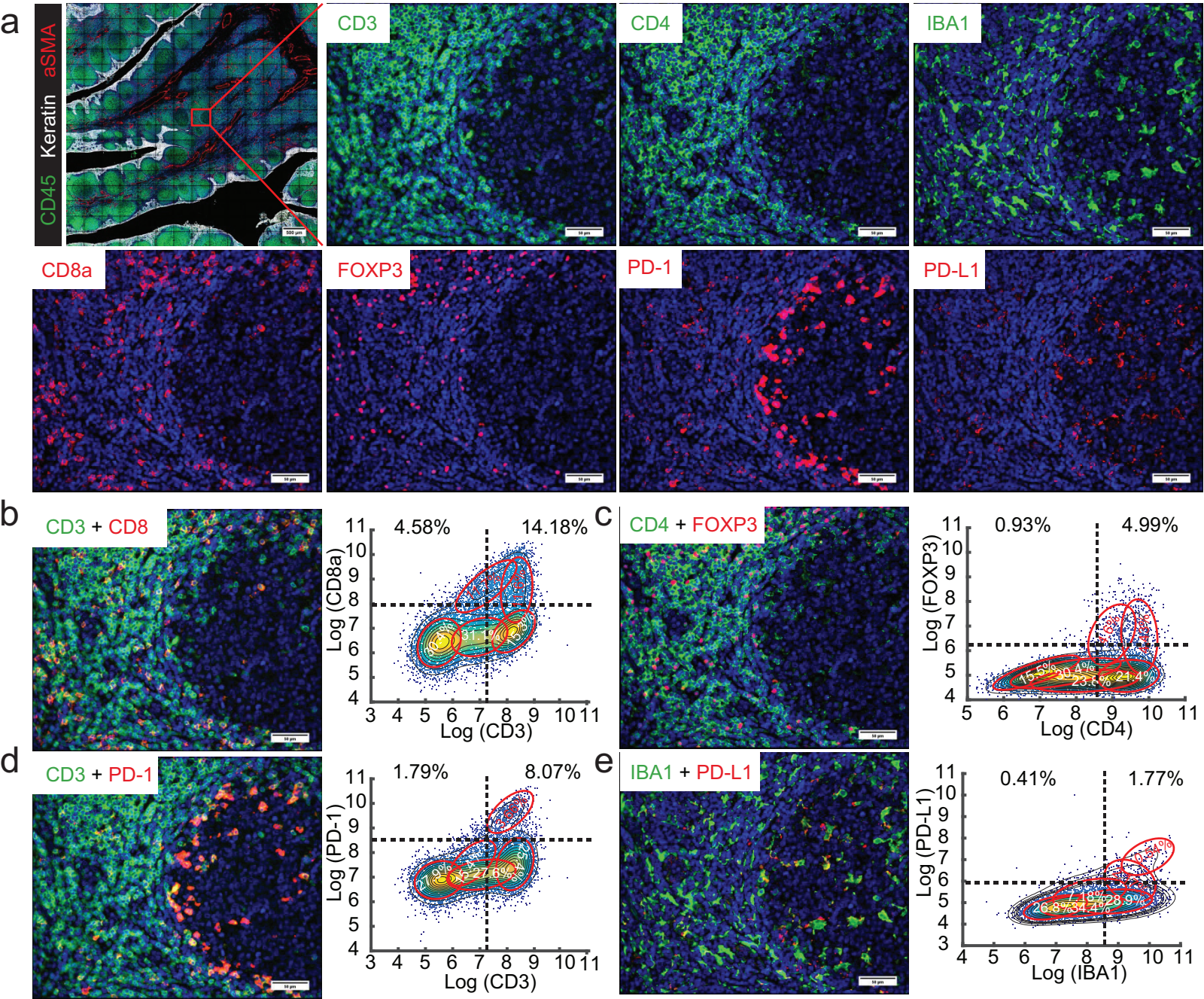

Figure-5 (Santagata)

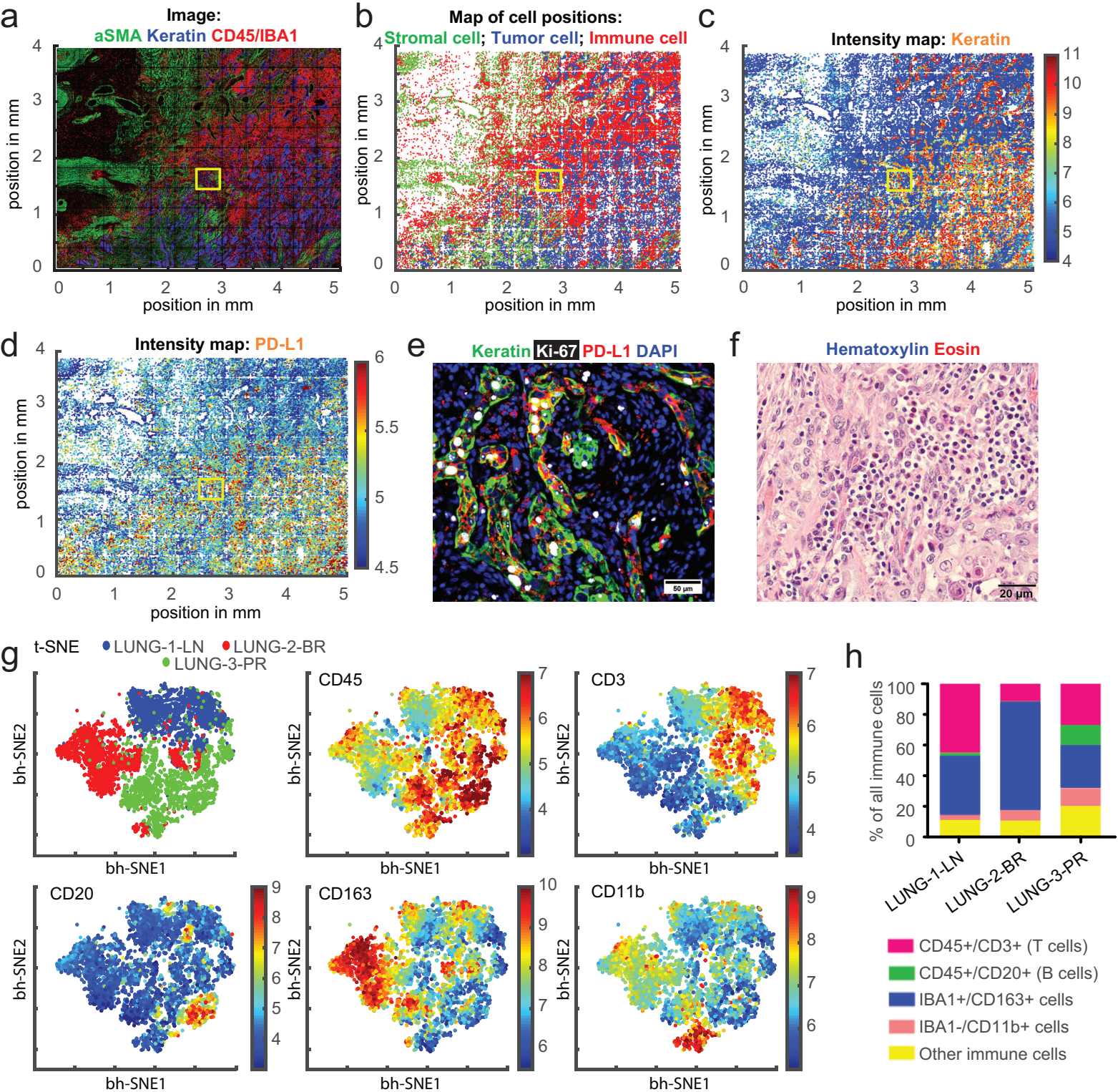

Figure-6 (Santagata)

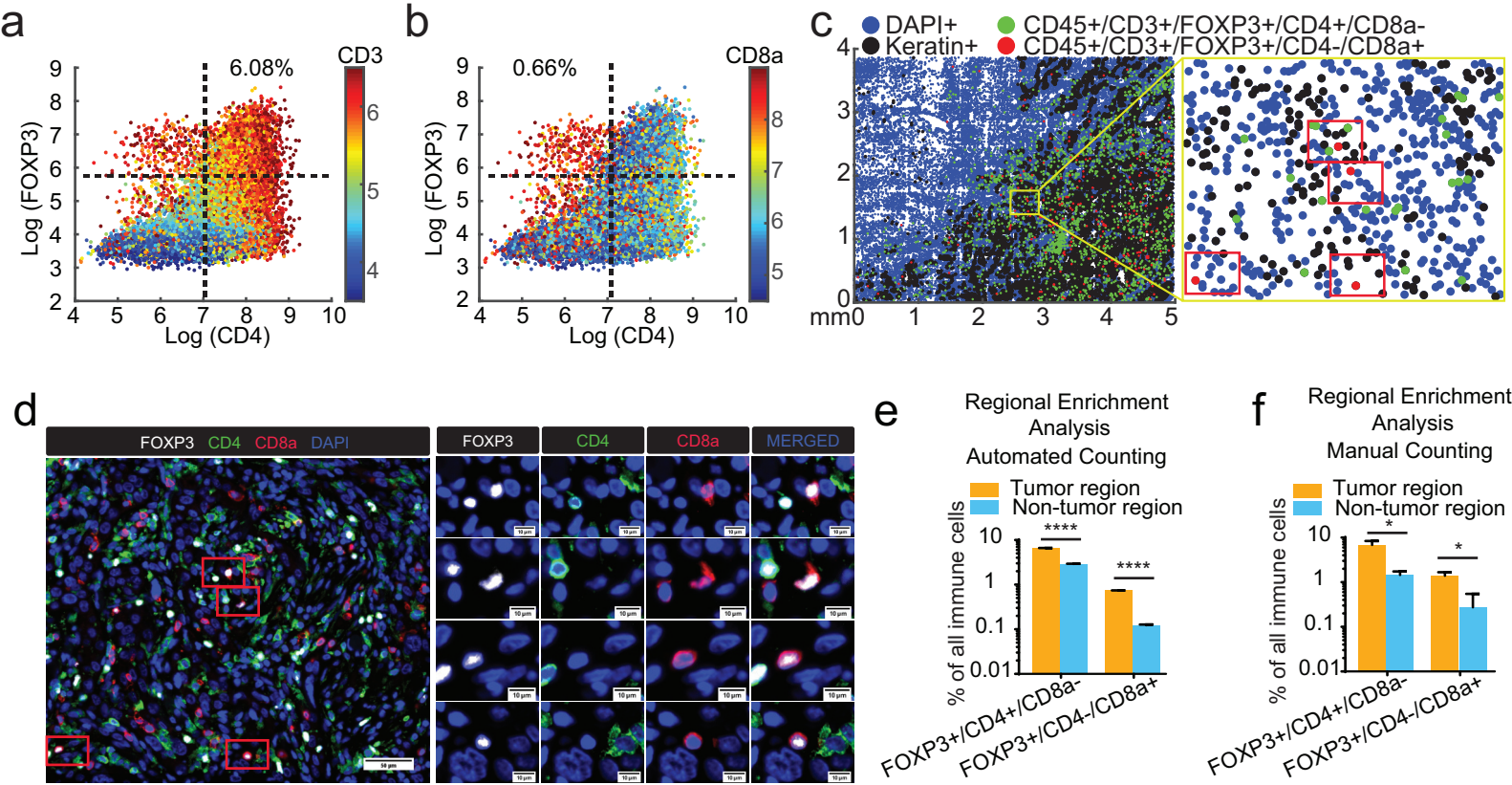

Figure-7 (Santagata)

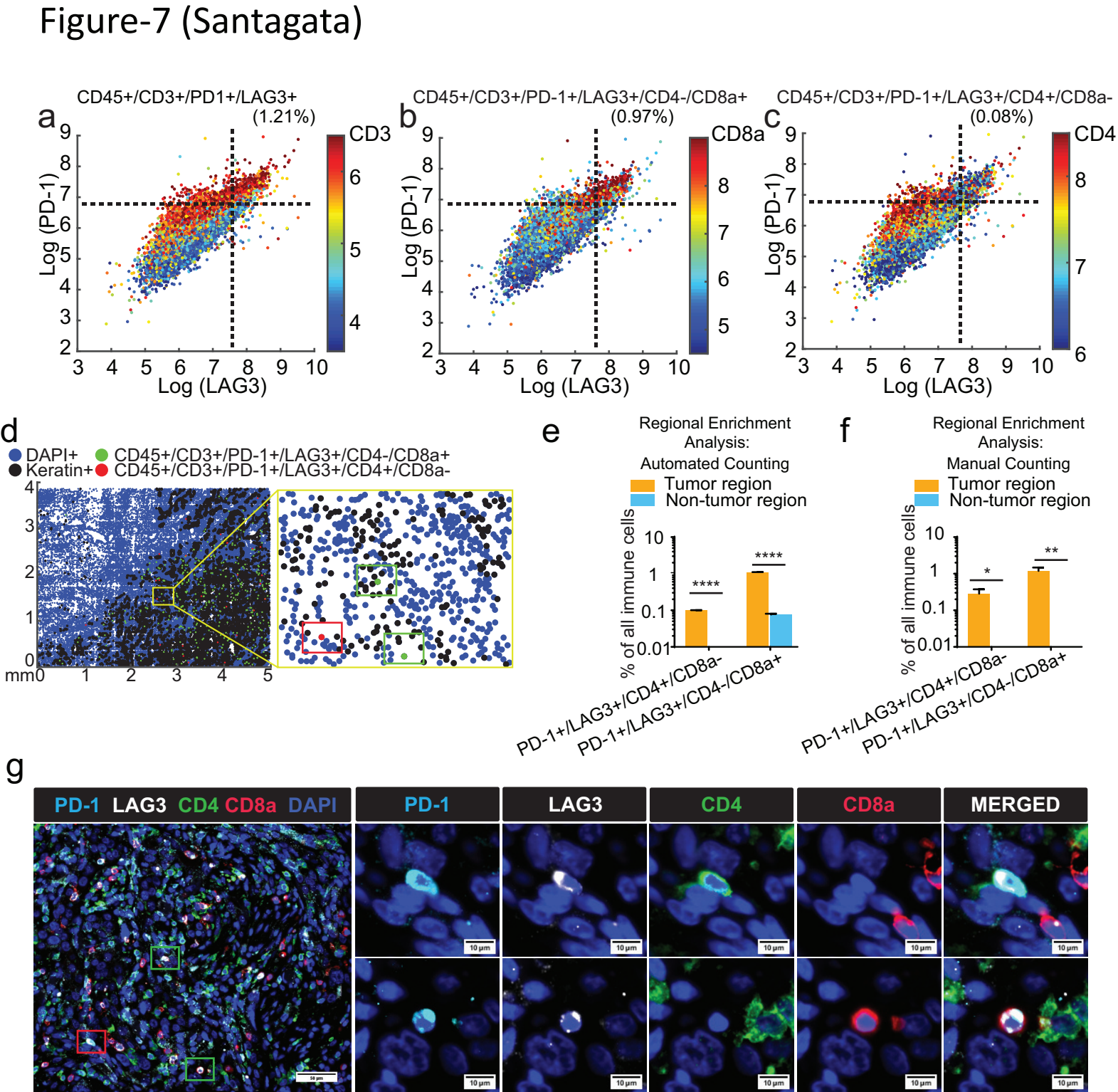

Figure-8 (Santagata)